To the University of Wyoming:

The members of the Committee approve the thesis of Christopher R. Cox presented on 17 May 2012.

Neil Humphrey, Chairperson

Snehalata Huzurbazar, External Department Member

Cliff Riebe

APPROVED:

Paul Heller, Head, Department of Geology and Geophysics

B. Oliver Walter, Dean, College of Arts and Sciences

Cox, Christopher R., Estimating thermal conductivities and melt water refreezing quantities from Greenland firn temperature profiles, M.S., Department of Geology and Geophysics, August, 2012.

Firn temperature profiles from the accumulation zone of the Greenland ice sheet are used to estimate thermal conductivities and melt water refreezing quantities. Firn thermal conductivity values are calculated from temperature profiles using a new optimization method. The results indicate that polar snowpack thermal conductivities may be significantly higher as a function of density than previously published empirical regressions would suggest. The quantity of melt water refreezing at each site is determined using temperature profiles and a heat conduction model. The heat conduction model is used to partition the seasonal heating of firn into heat conducted from the surface and heat released during refreezing. The heat from refreezing is then converted to a quantity of water using the latent heat of fusion. The refreezing values can be used to verify previously published refreezing estimates, thereby helping reduce uncertainty in Greenland surface mass balance calculations.

ESTIMATING THERMAL CONDUCTIVITIES AND MELT WATER REFREEZING QUANTITIES FROM GREENLAND FIRN TEMPERATURE PROFILES

by

Christopher R. Cox

A thesis submitted to the
Department of Geology and Geophysics
and the
University of Wyoming
in partial fulfillment of the requirements
for the degree of

MASTER OF SCIENCE
in
GEOLOGY

Laramie, Wyoming
August 2012

Copyright © 2012

by

Christopher R. Cox

Contents

List of Figures

List of Tables

Acknowledgments

I would like to thank my committee for their guidance and recommendations. I would also like to thank friends and family for reviewing early drafts of this thesis and providing helpful suggestions.

Christopher R. Cox

University of Wyoming
August 2012

Chapter 1

Introduction and Background

1.1 Introduction

The Greenland ice sheet covers an area the size of the western United States and influences climate, sea level, and ocean dynamics (*Cuffey and Paterson*, 2010). It is therefore critical to monitor the ice sheet and determine how it might be changing. Ice sheet mass balance is a measure of all the yearly mass inputs and outputs, and is used to determine whether the ice sheet is growing, shrinking, or staying constant. In Greenland, this consists of all accumulation and ablation processes, including discharge of ice into the ocean by calving. With the exception of basal melting and calving, all accumulation and ablation processes occur at the surface of the ice sheet and make up the surface mass balance (SMB).

$$\text{Mass balance} = \text{SMB} - \text{basal melting} - \text{calving}$$

Surface mass balance contributes to roughly half of the overall mass balance and has high inter-annual variability (*Van den Broeke et al.*, 2009). Recent model based estimates of SMB indicate significant upward trends in melting and runoff since about 1990 (*Ettema et al.*, 2009). Overall mass balance is also highly variable from year to year, but has been trending negative in the most recent decade with mass losses in the range of 100 – 267 Gton/yr (*Box et al.*, 2006; *Van den Broeke et al.*, 2009). This trend has been independently verified from GRACE satellite measurements since 2003 (*Van den Broeke et al.*, 2009). If

current trends continue, Greenland mass loss will become the main contributor to sea level rise in the 21st century (*Rignot et al.*, 2011).

One significant source of uncertainty in SMB estimates stems from the refreezing of melt water. In some regions of the accumulation zone significant summer surface melting occurs. This melt water infiltrates into sub-freezing snow and firn where some, or all of it, refreezes. The infiltration process is still poorly understood. Nonetheless, it is estimated that almost half of the total melt water generated during the melt season refreezes (*Ettema et al.*, 2009). Additionally, in a warming climate, refreezing can act to buffer increases in runoff from increases in surface melting. This happens when the maximum amount of refreezing that is possible has not yet been reached in an area and increased melting is simply refrozen. If all other mass balance components stay constant, this effect moderates sea level rise. Despite recent advances in high resolution climate modeling (*Ettema et al.*, 2010), modeling of the refreezing process remains overly simplistic and unverified.

This work presents two new ways in which temperature profiles can be used to better understand the refreezing process. In chapter 2, a new method is presented for calculating firn thermal conductivities using temperature profiles. These thermal conductivities are then used to establish a more accurate relationship between density and thermal conductivity in polar snow packs. Future studies can use this relationship to model heat flow more accurately, increasing the confidence in model based estimates of refreezing. Chapter 3 introduces a new method for estimating the amount of melt water refreezing in the firn using temperature profiles. Temperature profiles provide one of the only means of estimating refreezing from observed data. In contrast, previous refreezing estimates in Greenland have been based solely on unverified snow models and parameterizations. Given the potential significance of refreezing on SMB in Greenland, this new method provides an important means of testing the accuracy of refreezing estimates currently in the literature. Together, these methods will help to reduce the uncertainty in SMB estimates.

1.2 Background: Polar Snow Properties

On any glacier or ice sheet, the accumulation zone, by definition, is the region where there is a net gain in mass annually. However, varying degrees of surface melting and mass loss do occur seasonally in the accumulation zone. To some extent, the physical and thermal characteristics of the snowpack in different parts of the accumulation zone are a reflection of the amount of melting and refreezing that takes place.

Benson (1962) was the first to subdivide the accumulation zone into regions with similar physical characteristics. Benson applied many of the principles of sedimentology to snow and described regions in terms of "facies". The facies designation seems to be falling out of use and the different sub–regions of the accumulation zone are now commonly also referred to as "zones". The dry snow zone is the coldest and highest elevation sub-region of the accumulation zone. Here, virtually no surface melting takes place and the firn has not experienced diagenetic changes from liquid water infiltration. Stratigraphic structure results primarily from density variations due to new snow deposition by storms or wind. The dry snow zone is the largest subdivision of the accumulation zone in Greenland (*Janssens and Huybrechts*, 2000), however, the size of any particular zone varies across the earth and may not even be present on many lower latitude glaciers. At elevations below the dry snow zone, significant surface melting causes infiltration of liquid water into the firn. In the percolation zone, the infiltrating water refreezes and creates a heterogeneous distribution of ice layers and vertical channels. Additionally, the refreezing water releases latent heat that creates thermal perturbations in the snow. The percolation zone transitions to the wet snow zone once the entire snow pack becomes wetted by melt water. Finally, near the ablation zone, the slush zone is reached when the firn is saturated to capacity by melt water (*Benson*, 1962; *Janssens and Huybrechts*, 2000). The equilibrium line altitude (ELA) is the dividing line between the accumulation zone and the ablation zone.

Enough melting takes place in the lower part of the accumulation zone that some of the melt water may become runoff via transport through the ablation zone and off the ice, or, perhaps, by reaching the base of the ice through an englacial conduit. The runoff limit is the dividing line between where all melt ultimately refreezes and where some of

it begins to contribute to runoff. However, recent observations suggest that melt water is able to heterogeneously penetrate the firn to depths greater than 10m and remain mobile throughout the winter (*Humphrey et al.*, 2012). Therefore, the location of the runoff limit is not known very precisely at present, and it remains unclear how much melt water may be escaping from the accumulation zone.

1.2.1 Snow Thermodynamics

Pure snow is a porous medium consisting of a collection of ice grains of highly variable geometries and inter-granular bonding. At the higher densities characterizing firn, the individual grains become less distinct and the snow is more of an ice matrix with inclusions of air. Heat is conducted through both the ice skeleton and, to a lesser extent, the air in the pore space. However, overall heat conduction in snow is more complex than other porous mediums, such as sand, due to the effect of latent heat transfer and snow metamorphism. Latent heat transfer occurs when water molecules sublimate from one ice grain and are re-deposited on an adjacent grain. Temperature gradients in the snow help drive this process by creating vapor density gradients. Vapor transport also changes the snow crystal structure and degree of inter-granular bonding leading to snow metamorphism. These micro-structural changes due to metamorphism have a direct influence on thermal conductivity. This creates a positive feed back loop between snow metamorphism and heat transfer.

The overall measured snow thermal conductivity is referred to as the effective thermal conductivity (K_{eff}) as it encompasses the effects of both conductive and latent heat transfer. *Sturm et al.* (1997) summarizes the myriad studies that have measured K_{eff} in both laboratory and field settings. Almost all empirical studies relate the measured K_{eff} to snow density as it is a fairly easy to measure quantity in the field. However, a given snow density can exhibit a relatively wide range of snow microstructures resulting in a range of observed K_{eff} values (*Arons and Colbeck*, 1995). Furthermore, K_{eff} also has a temperature dependence that results from both the temperature dependence of conduction through the ice/air, as well as, the influence of temperature on vapor pressure and, therefore, latent heat transfer. Nonetheless, a variety of regressions of K_{eff} as a function of density have been published (See

Sturm et al. (1997)) and are useful given a lack of techniques to more accurately characterize the snow microstructure in the field.

Several relatively simple theoretical models relating density to thermal conductivity have been derived (*Arons and Colbeck*, 1995; *Carson et al.*, 2005). Most of these theoretical models neglect latent heat transfer and therefore do not predict K_{eff} directly, but they do provide a framework for comparing different empirical regressions. The most simple of the theoretical models are the parallel and series plate models. In both of these models the snowpack is idealized to consist of alternating layers of ice and air oriented parallel or perpendicular (series) to heat flow. Since thermal conductivity is analogous to electrical conductivity, it may be no surprise that the parallel and series models are equivalent to combining electrical conductors in parallel or series (see Appendix). Furthermore, more analytically complex models can be derived following the work of Maxwell for non-homogeneous electrical conductors (*Carson et al.*, 2005). *Schwerdtfeger* (1963) adapted Maxwell's work for an idealized snowpack consisting of an ice matrix embedded with spherical pockets of air. Figure 1.1 shows three theoretical models, as well as, the *Sturm et al.* (1997) regression. In general, the parallel and series plate models are thought to provide upper and lower boundaries on thermal conductivity respectively (*Carson et al.*, 2005), and, for the most part, empirical measurements confirm this to be the case (*Sturm et al.*, 1997).

1.2.2 Snow Hydrology

Anytime surface melt water is generated in the accumulation zone, it immediately infiltrates into the snow pack as saturated or unsaturated flow. Sub-freezing snow temperatures initiate melt water refreezing during infiltration and the refreezing rate is governed by the rate at which the heat given off during refreezing can be conducted into the surrounding snowpack (*Pfeffer and Humphrey*, 1998). This competition between infiltration rate and refreezing rate creates a complex hydrology.

Melt water infiltration, whether saturated or unsaturated, has two modes: uniform or heterogeneous. A uniform wetting front penetrates the underlying snowpack somewhat evenly in all directions. This type of infiltration has been described as piston or plug flow in

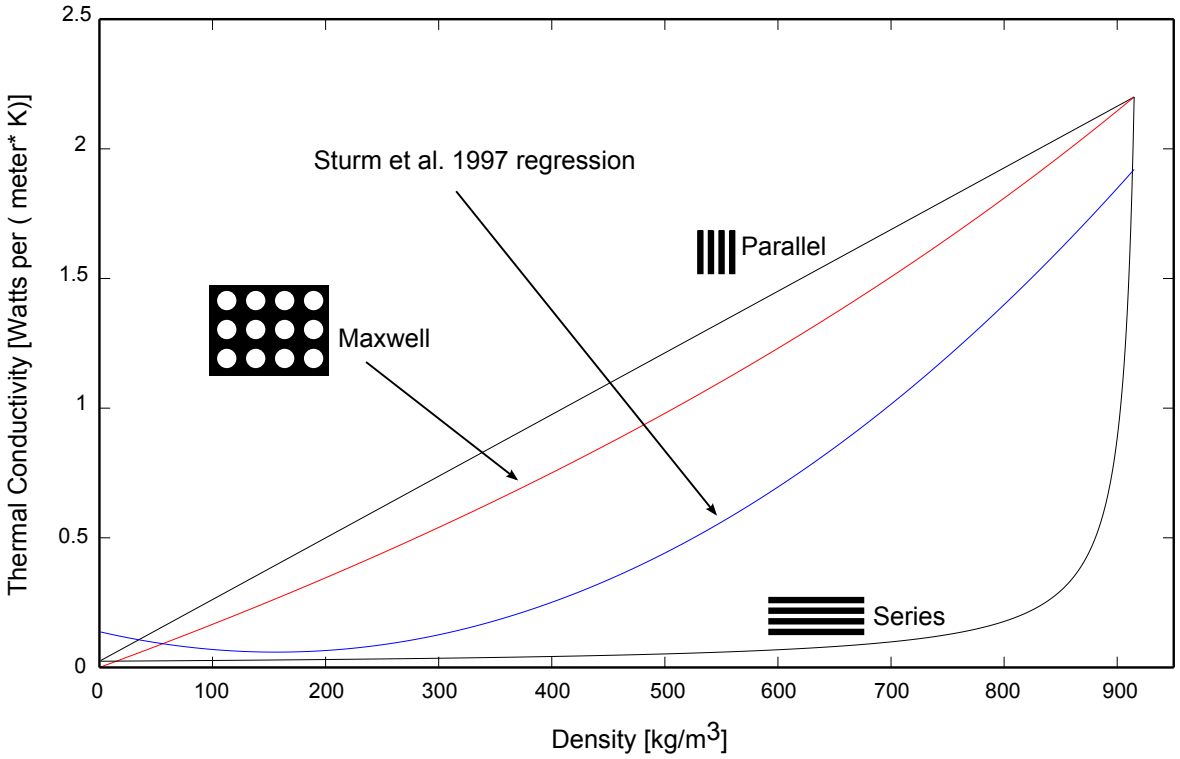

Figure 1.1: Theoretical and empirical relationships between density and thermal conductivity. The theoretical relationships are analytically derived from the simplified snow geometries described in the text. Also shown is a regression by Sturm et al. 1997, based on a compilation of hundreds of thermal conductivity measurements.

the vadose zone hydrology literature (*Hornberger et al.*, 1998). Here, the flow rate is described using Darcy's Law for both saturated and unsaturated flow (*Pfeffer and Humphrey*, 1996). A more heterogeneous mode of infiltration forms from both flow instabilities at the lower edge of the wetting front and underlying structures within the snowpack (*Armstrong and Brun*, 2008; *Pfeffer and Humphrey*, 1998). Termed "finger flow" or "piping", here the flow becomes isolated into multiple, isolated vertical channels. These vertical channels transport water much deeper into the snowpack than would otherwise be possible through purely uniform infiltration, but quantification of this process has yet to be achieved.

In both modes of infiltration, the downward movement of water can become impeded by hydrologic barriers such as buried wind layers, ice layers or density changes. A common barrier in unsaturated flow is a transition from fine to coarse grain size snow. During unsaturated flow, capillary forces in the smaller void space, fine grained snow prevent water from entering the coarse grained layer (*Hornberger et al.*, 1998; *Pfeffer and Humphrey*, 1998). If the infiltration rate is such that the barrier cannot be overcome before refreezing, a new ice layer will form at the boundary. Ice layers can help to initiate future pipe flow by creating an uneven surface that acts like a small catch basin where water can converge and ultimately flow downward in small high discharge regions (*Pfeffer and Humphrey*, 1998).

The mode of infiltration may also influence the degree of surface melting. For example, imagine two identical snow packs with the same surface heating. In the first snow pack, melt water infiltrates uniformly near the surface and then refreezes, warming the upper snowpack. Subsequent melting then occurs more readily with the warmer snow temperatures at the surface. In contrast, in the second snow pack, melt water is piped deeper into the snow and refreezes. Now the heat has less of an effect on near surface snow temperatures and less surface melt occurs because more energy must utilized to warm the relatively cold snow. A better understanding of melt water infiltration is needed in order to evaluate the significance of this effect.

1.2.3 Temperature Profiles

In Greenland, the snow in the accumulation zone is mostly below 0 °C due to sub-freezing mean annual temperatures. In the near surface, firn temperatures tend to resemble the surface air temperature while the air temperature is below 0 °C, and then remain fixed at the freezing point when melting is taking place. At depths beyond about 10m, temperatures become less variable and are roughly equal to the mean annual temperature (figure 1.2). In Greenland, where the lack of topography and vegetation results in fairly uniform surface heating, melting, and infiltration of melt water, heat transfer is primarily one dimensional in the vertical direction. This helps explain the general shape of temperature profiles. Heat is conducted into and out of the snowpack from the surface on daily and annual time scales. The daily heat wave is attenuated in about a meter, but the longer wavelength annual temperature cycle can influence the upper 10 - 20m of snowpack (*Cuffey and Paterson*, 2010).

An analytical solution to the heat equation can be found if the surface temperature variation is approximately sinusoidal (*Cuffey and Paterson*, 2010). In figure 1.2, a theoretical temperature profile, derived using the heat equation, is plotted with observed temperature data. The mid-winter theoretical profile is very similar to the observed temperatures on May 1. In contrast, the summer theoretical profile is much cooler than the observed temperatures in August. While this comparison is primarily aimed at explaining the general shape of the observed temperatures, the difference between the theoretical and observed summer profiles is, at least in part, due to added heat from refreezing. Refreezing in the near surface may even warm the first meter or so of snow to the melting point. Isolated refreezing events create temperature spikes that slowly diffuse into the surrounding snow pack (figure 1.2).

1.3 Field Methods

The temperature profile data used in this study was collected between 2007 and 2009 from a transect of 11 sites in southwestern Greenland about 100 km northeast of Jakobshavn Isbræ(Figure 1.3). This area of the ice sheet has seen numerous scientific expeditions including

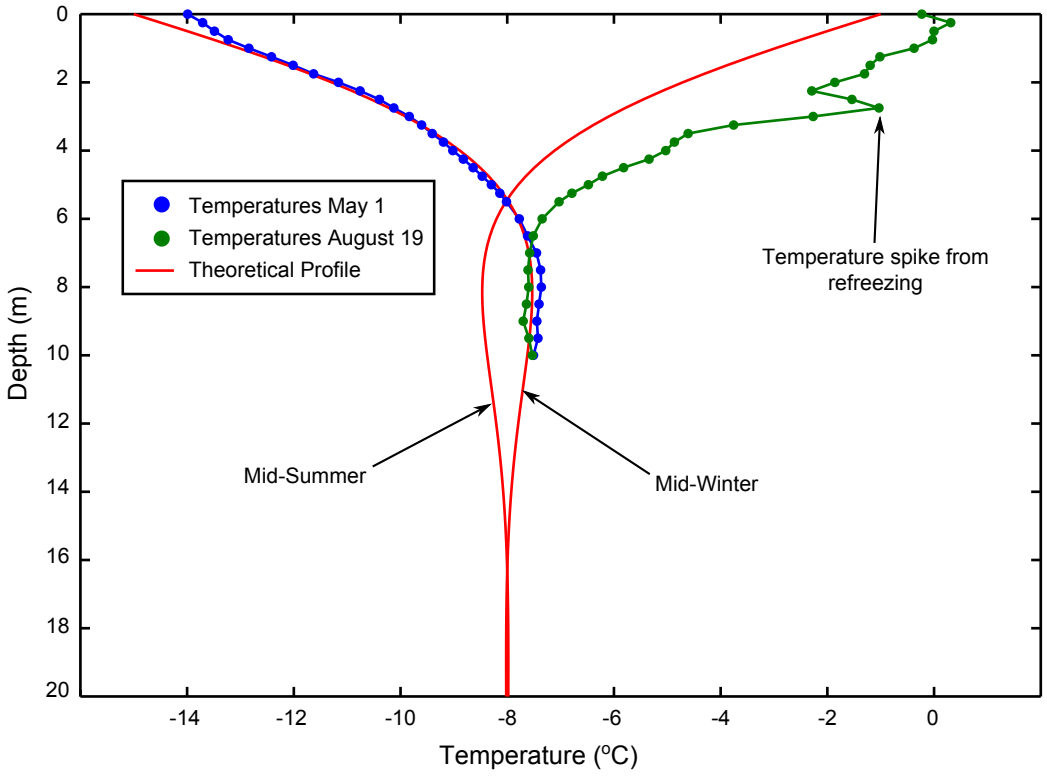

Figure 1.2: Temperature profiles from site H1 plotted with theoretical temperature profiles derived from an analytical solution to the heat equation with a sinusoidal boundary condition. The theoretical profiles help explain the general shape of the observed temperature data. An isolated refreezing event is created a temperature spike in the August profile.

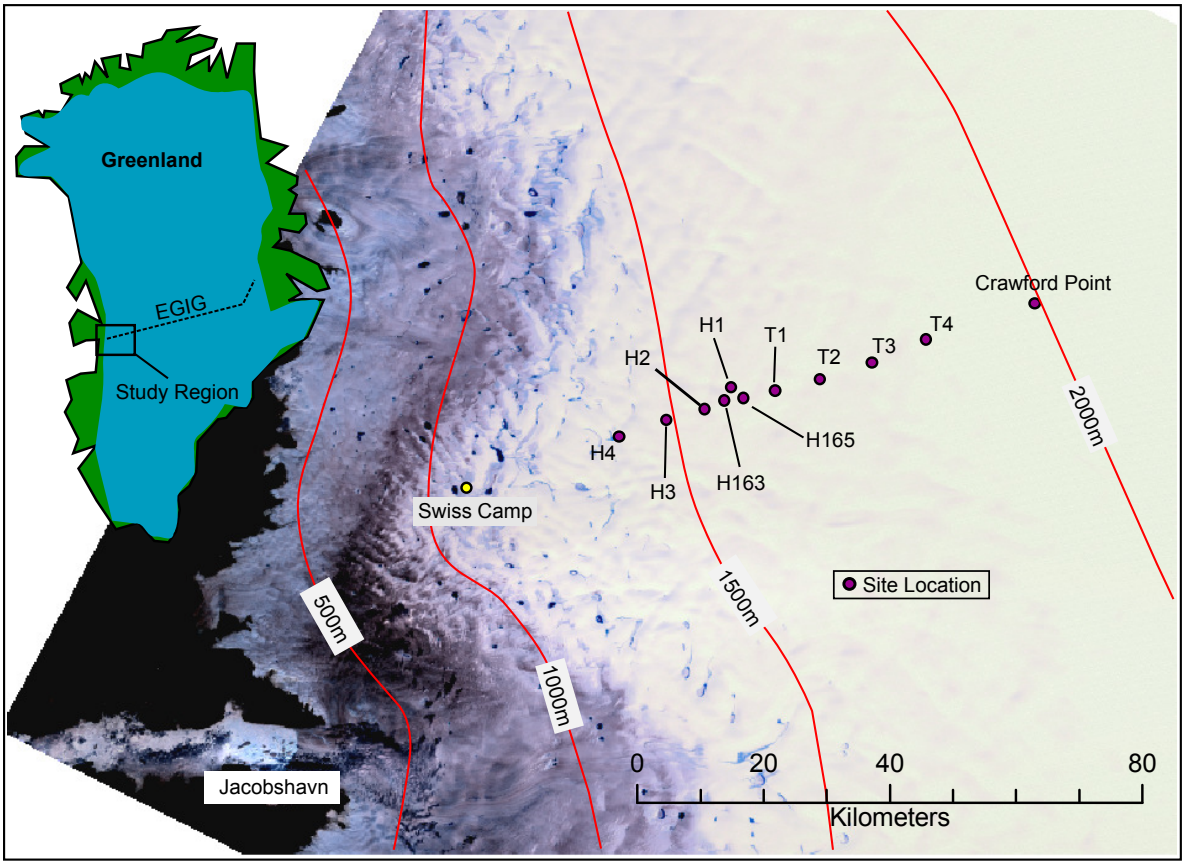

Figure 1.3: Map showing the study region in western Greenland. At each site (purple dots), a temperature string was installed in the firn to a depth of 10m.

Benson's 1955 traverse (*Benson*, 1962). The transect lies along a portion of the EGIG line, a route established in 1959 as part of an international scientific collaboration (*Finsterwalder*, 1959). Crawford Point (CP) lies near Eismutte, a camp established by Alfred Wegener in his ill-fated 1930 expedition.

1.3.1 Site Characteristics

All of the sites are within the the percolation and wet snow zones. The lowest elevation site (H4) is near the ELA and the highest elevation site (CP) is near the dry snow zone. Surface height increases at CP, as measured by a Greenland Climate Network automatic weather station (*Steffen et al.*, 1996), are on the order of a meter per year between spring of 2007 and spring of 2009. This is similar to annual accumulations reported by *Parry et al.*

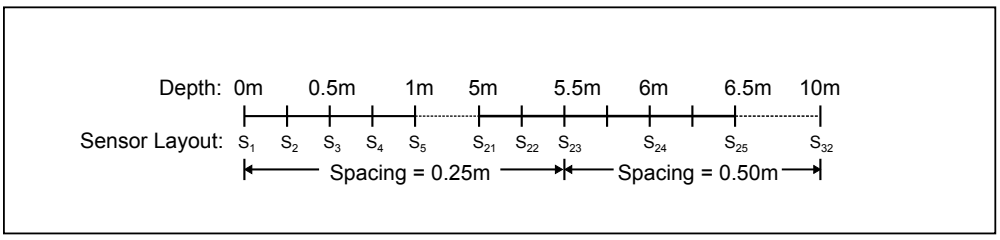

Figure 1.4: Diagram showing the location of the 32 sensors on each temperature string.

(2007) in the same area in 2004 as well as other observational and model based studies (*Benson*, 1962; *Hanna et al.*, 2006). Inter-annual variability and model resolution preclude any interpretations of small-scale accumulation trends along the transect. In contrast, it is clear that summer melting along the transect increases towards the ice margin both as a result of increasing temperatures associated with decreased elevation, as well as, changes in surface albedo due to decreases in snow cover.

2007 was a record high melt season in Greenland as indicated by both remote sensing and large-scale modeling. The extent and number of days when melt is occurring in Greenland can be determined using satellite observations of snow microwave emissions. *Tedesco et al.* (2011) uses satellite observations to calculate a seasonal melt intensity index that is a function of melt days and area melted. The 2007 melt index is the second highest over the period of record 1978-2010. Furthermore, high resolution climate modeling by *Ettema et al.* (2009) shows that 2007 had the lowest surface mass balance since at least 1958. In contrast 2008 was a more or less average year in terms of melting (*Tedesco et al.*, 2011).

1.3.2 Data Collection and Quality

Each site along the transect was instrumented with 32 temperature sensors to a depth of 10m (figure 1.4). Sensor spacing is 25cm from 0 to 5.5m and 50cm from 5.5 to 10m depths. To install the temperature strings, a 9cm Kovacs core drill was used to extract a 10m core from the firn. The temperature strings were then lowered into the hole and the remaining space back filled with cold snow. Stratigraphy and density measurements were taken from the core during extraction. After emplacement, the temperature readings stabilized after less than a day (*Harper et al.*, 2011). Sensor accuracy is estimated to be

about 0.25 degrees, but thermister aging and electronic noise decreases this accuracy to about 0.5 degrees. Furthermore, some of the sensors may be offset by around 0.5 degree due to mis-calibration (N. Humphrey personal communication). The accuracy of the density measurements in the core data is likely to be no better than about +/- 10 $\frac{kg}{m^3}$. This is especially true in the upper 1m of snowpack where lack of cohesiveness and surface melting made it difficult to obtain a sample for measurement (*Harper et al.*, 2011).

Not all sites were instrumented at the same time, for the same period, or with exactly the same sampling interval (Table 1.1). The upper sites from CP to T1 recorded data in the summer and fall of 2007, while the lower sites from T2 to H4 recorded data from the summer of 2008 to the spring of 2009. Most of the summer time data has a 20 – 30 minute sampling interval. Power requirements limited the sampling interval of the 2008/2009 winter data to every 8 hours. Finally, condensation on the data loggers in 2007 caused some of the data to be unusable.

Table 1.1: Temperature Profile Data Summary

Site	Latitude (N)	Longitude (W)	Elevation (m)	Data Dates	Sampling Interval	Data Quality
CP	69.8765	47.0102	1997	6/25/07-10/21/07	30 min	Good
T4	69.819983	47.4505	1877	7/3/07 - 1/27/08	30 min	Poor Sept-Jan
T3	69.7836	47.670183	1819	6/25/07 - 1/2/08	30 min	Good
T2-07	69.756933	47.880283	1750	6/28/07 - 10/29/07	30 min	Good
T1-07	69.738017	48.060967	1710	6/28/07 - 12/22/07	30 min	Poor Sept - Dec
T2-08	69.756933	47.880283	1750	5/27/08 - 5/16/09	20m, 8h Oct-Apr	Good
T1-08a	69.738017	48.060967	1710	5/30/08 - 5/16/09	20m, 8h Oct-Apr	Two bad sensors
T1-08b	69.738017	48.060967	1710	6/1/08 - 5/16/09	20m, 8h Oct-Apr	Excellent
H1	69.739083	48.2403	1680	5/31/08 - 5/15/09	20m, 8h Oct-Apr	Excellent
H163	69.72505	48.1902	1660	5/30/08 - 5/15/09	20m, 8h Oct-Apr	Excellent
H165	69.719783	48.2674	1644	5/30/08 - 5/15/09	20m, 8h Oct-Apr	Excellent
H2	69.706167	48.344967	1555	5/30/08 - 5/15/09	20m, 8h Oct-Apr	Excellent
H3	69.687433	48.499667	1540	5/31/08 - 5/17/09	20m, 8h Oct-Apr	Excellent
H4	69.660183	48.68945	1401	5/31/08 - 5/15/09	20m, 8h Oct-Apr	Excellent

Chapter 2

Thermal Conductivities

2.1 Introduction

Physically based models of snow subsurface processes are being used with increasing frequency to estimate refreezing quantities in SMB studies (*Bougamont et al.*, 2005; *Ettema et al.*, 2010). These models simulate both infiltration and heat flow to determine the amount of refreezing taking place throughout the snow pack. Model thermal conductivities are often calculated from snow densities using a regression by *Sturm et al.* (1997) (*Bougamont et al.*, 2005; *Wright et al.*, 2007). While this regression is based on an extensive data set, most of the measurements used in it correspond to lower density seasonal snow. However, in the accumulation zone of Greenland, the firn commonly reaches higher densities as it is gradually transformed to ice. Using any seasonal snowpack thermal conductivity regression on polar snowpacks may be fraught with error because there is no data to constrain these regressions at higher densities. Additionally, heat flow through high density snow is likely intrinsically different from low density snow due to changes in snow crystal geometry with increasingly large grain sizes and better bonding.

In this chapter, spatially variable thermal conductivities are calculated from temperature profile data via a new optimization method. The results are used to create a new relationship between firn density and thermal conductivities that is more appropriate for the higher density snow of polar regions.

2.1.1 History

A variety of field and laboratory methods have been used to measure the effective thermal conductivity of snow (K_{eff}). Several early studies through the first half of the 20th century (see *Brandt and Warren* (1997); *Sturm et al.* (1997)) estimated thermal conductivity from snow temperature profiles. Technology limited the spatial and temporal resolution of these early temperature profiles, and calculating K_{eff} from the temperature measurements required several simplifying assumptions. Nonetheless, this method, sometimes referred to as "phase shift" or "amplitude attenuation", provides some useful results and only requires temperature measurements at two depths. The basic idea behind the method is to assume that the daily or annual surface temperature cycle can be modeled as a periodic function. Then, if K_{eff} is assumed to be constant in both space and time, an analytical solution to the heat equation with a periodic boundary condition can be found. K_{eff} can then be constrained using temperature measurements at different depths to identify a phase shift or amplitude change in the temperature cycle (*Brandt and Warren*, 1997). The major error in this method stems from the simplifying assumptions, but wind pumping and penetration of solar radiation can also decrease the reliability of this method.

More modern measurements of thermal conductivities utilize a portable thermal probe device or are laboratory based (*Sturm et al.*, 1997). Portable instruments can be used in natural snow packs and are often considered more accurate than calculation from temperature profiles, but each measurement is representative of only a small sample in space and time. Laboratory based measurements use some sort of chamber where snow is subjected to thermal gradients or perturbations, and the response or steady state temperatures are used to calculate conductivities. In contrast to in-situ measurements, laboratory experiments often use artificial or aged snow that may not represent actual snowpack conditions.

Improvements in technology enable modern temperature profiles to have high spatial and temporal resolution. Also, the snow temperatures can now be continuously monitored for extended periods of time. These improvements give modern temperature profiles the potential to yield direct insight into long term snow thermal processes while being minimally invasive.

2.2 Inverse Theory

Calculating snow thermal conductivities from temperature measurements is an *inverse problem* because the measured temperatures are a function of the thermal conductivities. Inverse problems are particularly challenging because the solutions can often be non–unique and ill–posed (*Aster et al.*, 2005). A problem is non-unique if there are solutions besides the true solution that also solve the problem. For example, effective thermal conductivities are non–unique if they are variable with space and time. This makes sense intuitively because, when thermal conductivity can vary, the heat fluxes into and out of a region can be any value as long as the net heat flux is the same. In other words, a temperature change could be the result of heat moving through a region very rapidly or very slowly if the net change in heat is the same.

An ill–posed problem is one where a small error in the data has a large effect on the parameter being estimated. Even with highly accurate electronic temperature sensors, electronic noise and imperfect calibration of the temperature sensors creates almost imperceptible errors in the temperature profiles. These errors become magnified when the thermal conductivities are calculated and the resulting error can be of the same magnitude as the thermal conductivities themselves. Despite the challenges posed by inverse theory, the potential for insight into variations in snow properties using temperature profiles makes the complex analysis worthwhile.

2.2.1 Solution Strategies

There are a number of different techniques that could potentially be used to calculate thermal conductivities from temperature profiles. One seemingly straight–forward strategy is to solve for thermal conductivities using a linear approximation of the heat equation. The heat equation with variable thermal conductivity is as follows:

$$\rho(z)C\frac{\partial T}{\partial t} = \frac{\partial}{\partial z}(K_{eff}(z)\frac{\partial T}{\partial z}) \tag{2.1}$$

Here z is depth, C is heat capacity (assumed constant), and ρ is density as a function of depth. Importantly, K_{eff} is assumed to be constant with time, but that may not be

appropriate for a snowpack that is undergoing rapid metamorphism.

Equation 2.1 can be approximated at a point T_z (Figure 2.1) along a temperature profile using finite differences (see Appendix):

$$\rho_z C \frac{T_{z,t+\Delta t} - T_{z,t}}{\Delta t} = \left(\frac{K_{z+1}\frac{T_{z+1}-T_z}{\Delta z} - K_z\frac{T_z-T_{z-1}}{\Delta z}}{\Delta z}\right) \tag{2.2}$$

If T_z, T_{z+1}, and T_{z-1} all correspond to the location of observed temperatures and densities, then the only unknowns are the thermal conductivities. Applying equation 2.2 at all the temperature sensor locations along the profile yields a system of equations. The math of finite differencing is such that the unknown thermal conductivities correspond to locations between the temperature nodes (T_z). The result is $n + 1$ number of unknown thermal conductivities and n equations. This is an *under–determined* system of equations with an infinite number of possible solutions (*Aster et al.*, 2005). However, if the thermal conductivity values are assumed to remain constant over some range of time, equation 2.2 can be re–applied to the profile at a later time period. This creates a new set of equations, but the same number of unknown thermal conductivity values. Now the system is *over–determined* and a solution can be found by least squares methods.

Unfortunately, when this method was tested on noisy synthetic data, the calculated thermal conductivities were significantly different from the thermal conductivities used to make the synthetic data (discussed more in section 2.3.2). One reason for the lack of success in this method stems from the problem's ill-posedness. Even a relatively small amount of noise in the temperature data creates large errors in the calculated thermal conductivities. In the observed data there is always some random electronic noise and, more significantly, slight mis-calibrations of the temperature sensors. Often times these mis-calibrations are so small that they cannot be detected from visual inspection of the temperature profile. Another problem with this method is due to the lack of significant temperature variation at depth. If the temperatures stay more or less the same with time, there isn't much difference between some of the equations in the system, and this also creates error. Qualitatively, no new information is gained when the equations are basically the same. Clearly a more robust inverse method is needed.

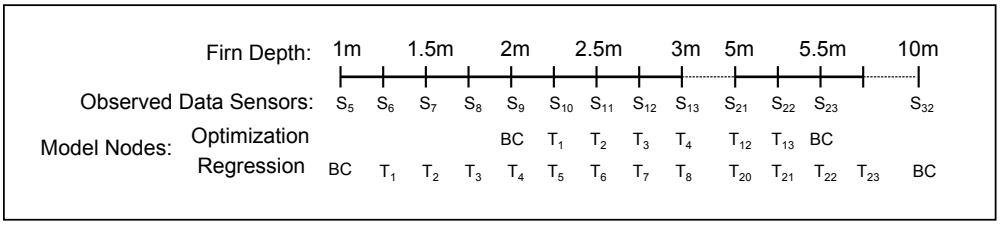

Figure 2.1: Diagram showing the location of the temperature sensors in the firn, as well as, the layout of the temperature nodes in the heat conduction models. The boundary conditions (BC) of both models are determined by observed temperature data.

2.3 Optimization Methods

An optimization scheme proved to be the most successful technique for estimating thermal conductivities using temperature profiles. This method utilizes a heat conduction model to iteratively test thermal conductivity values. At each iteration, a set of K_{eff} values are input into the model and the output temperatures are compared to the observed temperature data. An optimum set of K_{eff} values are found when the model output temperatures closely match the observed temperatures.

One benefit to this method is that errors in the temperature measurements have less of an influence on K_{eff} values because the values are not calculated directly from the temperature data. Furthermore, additional constraints, known as regularization, can be placed on the solution in order to find a more physically realistic solution.

Heat conduction is modeled from 2 – 5.5m depths using an implicit finite difference scheme with an hourly time step and a 0.25m nodal spacing (figure 2.1). The model domain is limited to this relatively narrow range of depths because the temperature sensor spacing in the observed data is also 0.25m from 2 – 5 meters. Also, the temperature sensors above 2m are avoided because they may be influenced by solar radiation and surface exposure. Model initialization and boundary conditions are taken from the observed data. With this setup, 13 interior temperature nodes are free to evolve over the course of the model run in response to the boundary conditions and 14 input thermal conductivities. At the end of the model run, the difference between the model output and the observed temperature data is used as a measure of the accuracy of the input thermal conductivity values.

The heat conduction model can be thought of as a vector function:

$$\mathbf{F}(K_{eff}) = T \tag{2.3}$$

A vector of K_{eff} values are input and a temperature profile T is output at the end of the model run. The optimization problem is to find the minimum of the difference between the model output temperature profile and the observed temperature profile. The 2-norm (see appendix) of the vector of differences serves as a scalar measure of the overall "model fit" to the observed data. The optimization problem can be written mathematically as:

$$min\ f(K_{eff}) \quad where \quad f(K_{eff}) = \|\mathbf{F}(K_{eff}) - T_{obs}\|_2^2 \tag{2.4}$$

Here the *square* of the 2-norm is minimized, as this is consistent with the numerical algorithms used to solve the optimization problem.

A solution to equation 2.4 can be found using the Levenberg-Marquardt (LM) method, in this case implemented in Matlab. LM is an iterative algorithm that begins with an initial guess of the optimum vector of K_{eff} values. The initial guess is unlikely to be the minimum of $f(K_{eff})$, so at each iteration LM numerically estimates the gradient of $f(K_{eff})$ and follows a path of steepest descent to find a minimum of $f(K_{eff})$ (*Aster et al.*, 2005). There are several potential pitfalls to using an optimization algorithm. The function $f(K_{eff})$ must be smooth and continuous, which is difficult to verify or visualize given that the function exists in 15 dimensional space. LM may also converge to a local minimum, or $f(K_{eff})$ may be relatively flat without a real clear minimum. Despite these dangers, the LM algorithm successfully found K_{eff} values where the the difference between the model output temperatures and observed temperatures is on the order of 10^{-10}.

2.3.1 Regularization

Given that there is error in the temperature measurements, it is undesirable to match the observed data too closely. Even if the K_{eff} values were known exactly, there would still be some difference between the model output and observed temperatures ($f(K_{eff})$ would be greater than zero) due to errors in the observed temperatures and numerical model.

This means there are a range of possible K_{eff} values such that the model and observed temperature differences are within the uncertainty of the temperature measurements. In order to find the best solution, further constraints must be imposed on the possible values of K_{eff}. This is known as regularization.

One common regularization technique is to think of the values of K_{eff} as a vector, and find the solution with the smallest 2-norm. A more physically based regularization technique is to find the solution that is smoothest with space. This would constrain the K_{eff} values to vary gradually along the profile, without any big jumps or discontinuities. However, there is no reason for the thermal conductivities to vary smoothly with space. In fact, sharp density contrasts and ice layers are likely to create a very discontinuous thermal conductivity profile.

I propose that the best solution is one where thermal conductivities vary smoothly as a function of density. A smooth relationship between thermal conductivities and densities is one where similar density layers have similar corresponding thermal conductivity values. For example, suppose two sets of thermal conductivity values are found for a particular site that both result in model output temperatures that are sufficiently close to observed temperatures. At most of the sites, the density profile will have layers with similar densities. The best solution is the solution where the thermal conductivities in these layers are also similar themselves.

A smooth K_{eff} – density relationship is not a guarantee, since there is a wide range of thermal conductivities possible for a given snow density (*Arons and Colbeck*, 1995; *Sturm et al.*, 1997). However, two layers from the same snowpack with the same density are likely to have experienced a similar temperature history. This results in snow metamorphism in both layers that converges to similar micro–structural geometries and thermal conductivities. Therefore, the most likely solution should be the one with less variability in K_{eff} values corresponding to similar densities.

This form of regularization is implemented by minimizing the variability in K_{eff} values for a narrow density range. Another way to describe the variability is to use $\frac{d^2K_{eff}}{d\rho^2}$, which is lower for a smoother curve and higher for a rougher curve. A crude approximation of $\frac{d^2K_{eff}}{d\rho^2}$ is easily calculated to measure the overall smoothness, or conversely "roughness".

Optimization with regularization can be implemented mathematically via a "damped least squares problem":

$$min\ (\|\mathbf{F}(K_{eff}) - T_{obs}\|_2^2 + \alpha^2\|R\|_2^2) \tag{2.5}$$

This formulation is simply equation 4 augmented with a component that accounts for the roughness in the K_{eff} density relationship. R is a vector of roughness values, and alpha is a weighting parameter. A large value of alpha results in an optimized solution that has less roughness (is smoother). However, the penalty for a smoother solution is an increase in the difference between model output temperatures and observed temperatures.

Equation 2.5 can again be solved using the Levenberg-Marquardt algorithm. Instead of just solving equation 5 once for a particular value of alpha, the algorithm is run several times with several of different values of alpha. By doing this, the tradeoff between model fit and smoothness can be explored and the best solution selected.

2.3.2 Synthetic Data Testing

Five synthetic temperature profile datasets were created to test the optimization method. The datasets were generated using the finite difference heat conduction model described in chapter 3. The model was run with an hourly time step for several months using realistic boundary and initial conditions for several different sites. All thermal conductivities in the model were calculated from profile densities using the *Sturm et al.* (1997) regression. The accuracy with which the Sturm regression can be reconstructed from the synthetic temperatures is indicative of the success of the optimization scheme.

Noise was added to the synthetic data prior to implementation of the optimization method. To simulate electronic noise, normally distributed random noise with a mean (μ) of 0 and a standard deviation (σ) of 0.05 °C was added to all the hourly temperature measurements. Additionally, to simulate mis-calibrated data, a normally distributed ($\mu = 0$, $\sigma = 0.05$) random offset was introduced into the entire temperature record of each sensor. Finally, normal random noise with a mean of 0 and a standard deviation of 10 $\frac{kg}{m^3}$ was also added into the densities profiles.

Figure 2.2 shows the roughness ($\|R\|_2^2$) and model fit ($\|\mathbf{F}(K_{eff}) - T_{obs}\|_2^2$) of different

optimized solutions for one of the synthetic datasets using alpha values ranging from 50 to 20000. The vertical axis is the norm of the roughness vector and the horizontal axis is the norm of the fit of the model to the synthetic data. As alpha is increased, the optimization solution is smoother (less rough), but has a worse fit to the observed data (increased 2-norm). This type of plot is known as an L–curve due to its shape and is usually constructed with a log–log scale. Both the synthetic and observed data, when analyzed using the optimization method, exhibit the characteristic 'L' shape, but only with linear axis (see figure 2.2 for example). The reasons for this are unknown, but the plot nonetheless illustrates the tradeoff between smoothing and model fit.

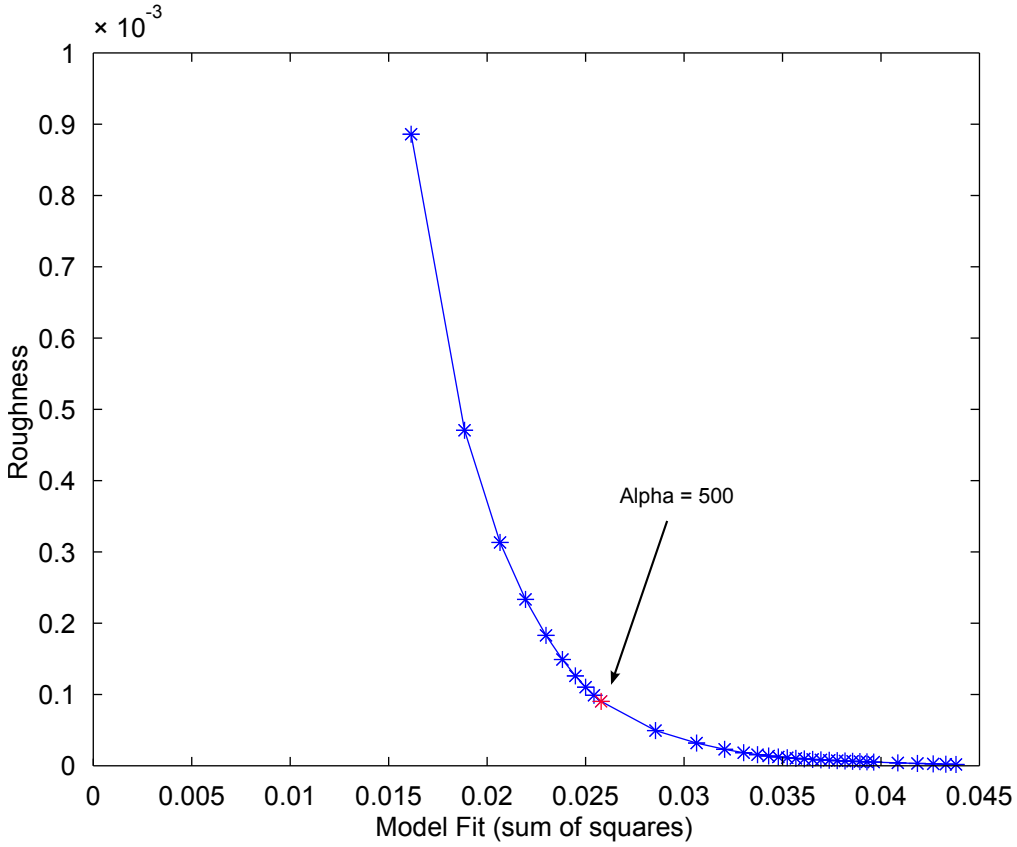

Figure 2.2: L–curve for one of the synthetic data sets. The best solution (with an $\alpha = 500$) corresponds roughly to the corner of the curve.

Given that the true thermal conductivities are known for the synthetic data (Ktrue), a measure of the difference between the optimized K_{eff} values and Ktrue can be calculated for each value of alpha. In this case, the most accurate model corresponds to an alpha

value of about 500. This value of alpha also happens to correspond closely to the corner of the L-curve. The L-curve corner is often used in inverse theory as a simple criterion of the best solution because it is a reasonable balance between under–fitting and over–fitting the data (*Aster et al.*, 2005). Not all the synthetic data sets resulted in the best solution corresponding to the L-curve corner, but were instead associated with very high values of alpha. Nonetheless, as shown in figure 3, using the L-curve corner criterion results in a fairly good match between the Sturm et al. regression and the final reconstructed thermal conductivities. Averaging the K_{eff} values to 25 $\frac{kg}{m^3}$ wide bins (red points) results in an even better match with the Sturm regression.

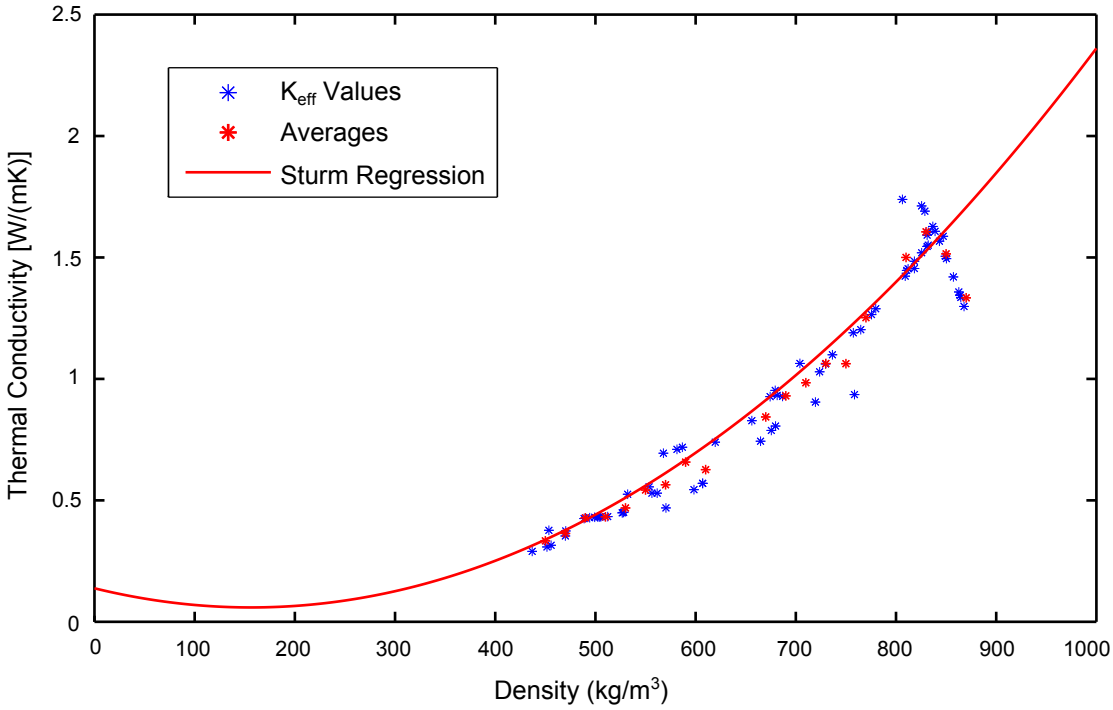

Figure 2.3: K_{eff} values from all synthetic temperature data sets as determined by the optimization method (blue), and their averages in 25 $\frac{kg}{m^3}$ wide density bins (red points). Also plotted is the Sturm regression used in the generation of the synthetic data.

2.3.3 Observed Data

The optimization method is applied to all sites with data from 2008-2009. This includes sites T1, H1, H163, H165, H2, H3 and H4. Only temperature measurements made outside

of the melt season (May to October) are used so that any influence of refreezing melt water is minimized. The 2007 sites are not used because the winter data usually spans less than one month worth of time. The sampling interval of the data loggers at the 2008/2009 sites varied between 20 minutes and 8 hours due to power requirements, so linear interpolation is used to create hourly boundary conditions at some sites. The densities used in the model are taken from firn cores extracted from each site. The L-curve corner criterion is used to determine the final optimal thermal conductivities at each site. At most of the sites, the corner corresponds to an alpha = 450. This value was also used at sites H165, H2, and H4, were the L–curve did not have a sharp corner.

2.4 Results

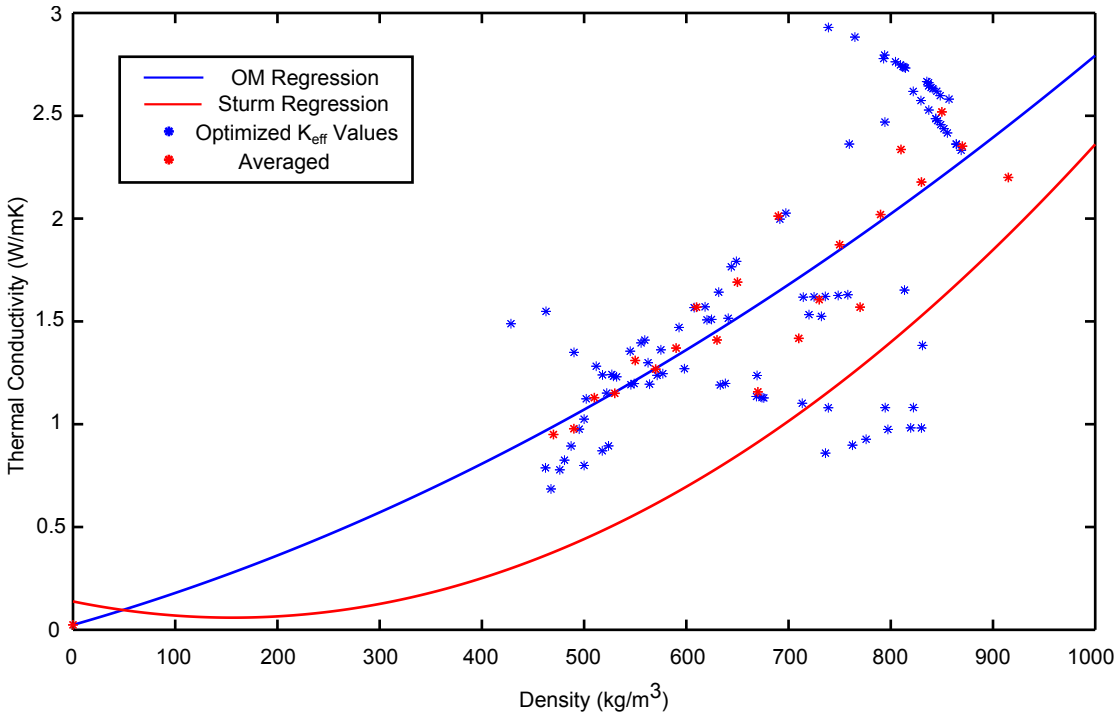

Figure 2.4: Optimal thermal conductivities from each site (blue). Average values are generated from all values inside 25 $\frac{kg}{m^3}$ wide density bins (red points). A quadratic regression is fit to the red points (OM regression).

There are two major clusters of optimized thermal conductivity values. The first cluster is centered on a density of about 550 $\frac{kg}{m^3}$ and the thermal conductivity values of this cluster

are well above the Sturm regression. There is a second cluster of values with densities around 850 $\frac{kg}{m^3}$. These values are associated with site H2 and H4. The linear structure seen in this clustering of values is likely an artifact of the smoothing bias. Finally, the scattered, unusually low values may be a result of the L-curve criterion failing to provide an adequate solution.

Given the uncertainty in the densities, the thermal conductivity values are averaged to 20 $\frac{kg}{m^3}$ density bins. A quadratic regression is fit to the averaged values using least squares techniques. Included in this regression are two endpoint constraints that are not derived from the optimization method. The first, at zero density, is the thermal conductivity of air. The upper end point is the accepted value of the thermal conductivity of ice (2.2 W/mK) at a density of 915 $\frac{kg}{m^3}$. This regression is referred to as the "optimization method regression" (OM) to distinguish it from other regressions. Overall, the OM regression has significantly higher values for a given density and much less curvature compared to the popular Sturm regression.

2.4.1 Regression Comparison

The accuracy of the OM regression is evaluated against theoretical thermal conductivity models and the Sturm regression using a second heat conduction model. Unlike the model used in the optimization procedure, the boundaries are extended to range from depths of 1 to 10m. Additionally, data from the 2007 sites, which is not used in the OM regression, is used to provide an independent source of model verification.

Four model runs are executed using the 2007 data from sites T4, T3, T2, and T1. Data from CP is not used as there is no density core associated with the temperature measurements there. The site densities are used to calculate thermal conductivities via the OM and Sturm regressions and the Maxwell and parallel plate theoretical models. The site temperature data is used for model initialization and boundary conditions. Finally model output temperatures are compared to the observed temperatures and the 2-norm of the temperature differences is used as a measure of model fit (see figure 2.5).

At all sites, model output temperatures using the OM regression are significantly closer

to observed values than temperatures output by the Sturm regression. In contrast, the OM regression is similar in performance to the theoretical models. This is not too surprising given the similarity between the OM regression and theoretical models (figure 2.6).

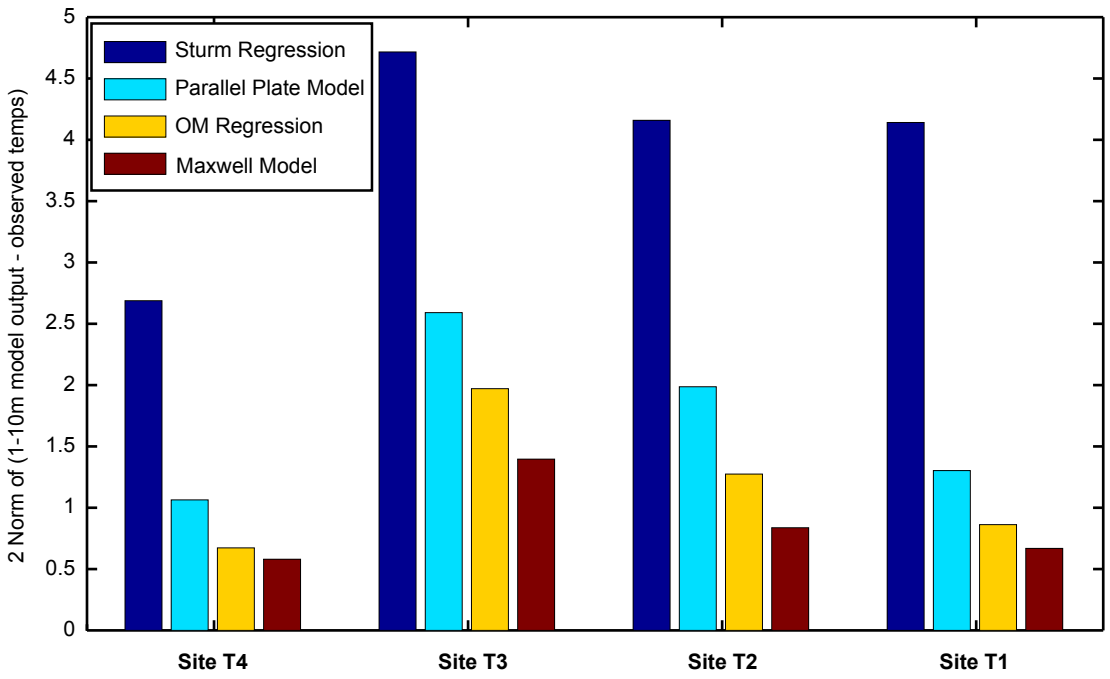

Figure 2.5: Comparison of the accuracy of regressions as measured by output model temperatures compared to observed temperatures. A lower 2-norm indicates less difference between the model output and observed data. The Maxwell theoretical model shows the best performance at each site.

2.5 Discussion

The Sturm regression is based on an aggregate of many previous studies, but focuses on seasonal snow with data concentrated in densities below 500 $\frac{kg}{m^3}$. In contrast, polar snow and firn is associated with higher densities due to multi-year compaction and refreezing. These new estimates indicate that for higher density snow and firn, the transition to higher thermal conductivities may be more rapid than would be expected by simply extrapolating lower density regressions. A sigmoidal type curve may be more representative of the entire density range.

There is a strong similarity between the OM regression and the Maxwell and Parallel

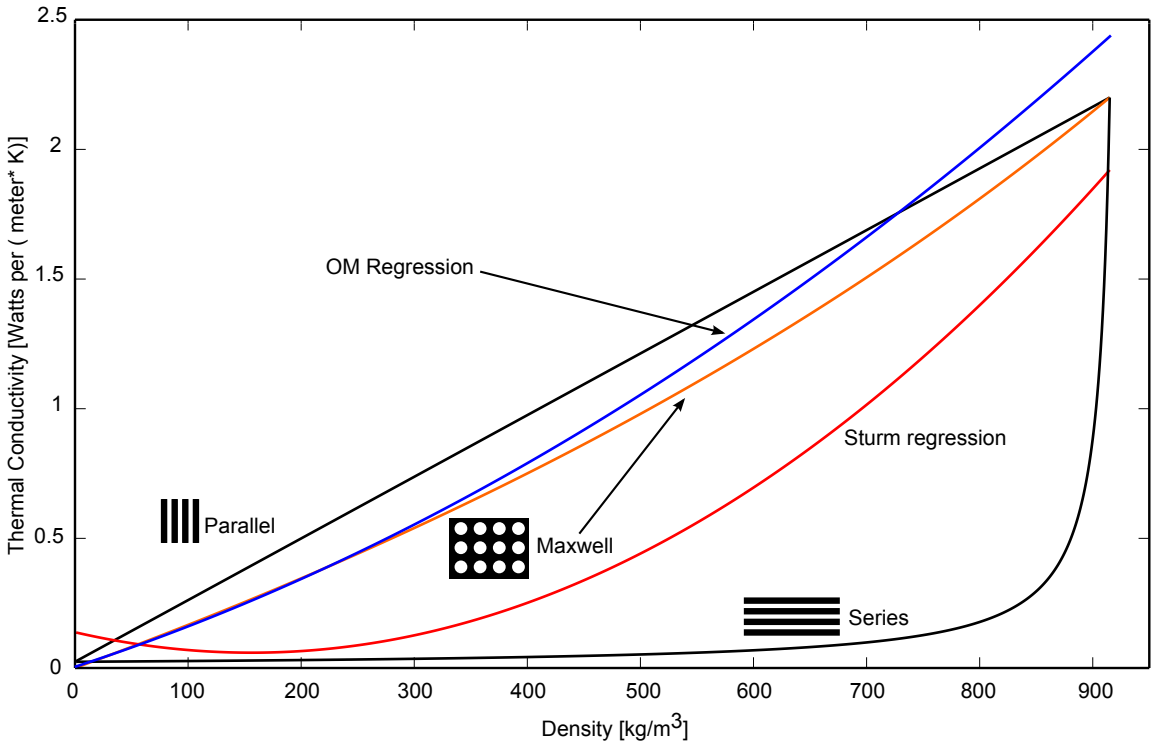

Figure 2.6: Comparison of OM regression to theoretical models and Sturm regression. The OM regression is quite similar to the Maxwell and Parallel Plate theoretical models.

plate theoretical models (figure 2.5). Indeed, given the uncertainty in the temperature and density data, there is likely no significant difference between the OM regression and these theoretical models. This may reflect a decrease in the variability of the firn microstructure at high densities. Vapor transport is also more limited as permeability decreases and latent heat transport, in turn, becomes less variable and significant. The snow is evolving towards a bubbly ice matrix and there is no room for large variations in crystal shape and inter–granular bonding. The result is a better agreement between theoretical and observed thermal conductivities at higher densities.

2.6 Conclusion

Calculating effective thermal conductivities from firn temperature profiles is challenging due to the ill-posedness of the problem. Electronic noise and offsets in the temperature readings from mis-calibration can create large errors in calculated K_{eff} values. The optimization technique provides a robust means of estimating thermal conductivities in the face of measurement error. The results show that in higher density snow packs and firn, the thermal conductivities may be higher than those predicted by extrapolation of low density regressions. Furthermore, the similarity between theoretical snow models and the OM regression shows that beyond about 500 $\frac{kg}{m^3}$ the snow pack evolves toward an ideal composition that can be modeled as a matrix of ice with pockets of air. Future studies in polar regions and higher density snow packs may consider using a regression that gives higher values of thermal conductivity than those commonly used in seasonal snow packs.

Chapter 3

Refreezing Quantities

3.1 Introduction

Refreezing is difficult to quantify because it is both poorly understood and heterogeneous. There are currently no means of directly measuring refreezing quantities. Seasonal densification of the snowpack gives some indication of the amount of mass refreezing in the snow, and this has been investigated by *Parry et al.* (2007). They found that over the course of the melt season, the upper snowpack shows density increases on the order of 30 to 50%. However, changes in snow densities also result from compaction and metamorphism, making it difficult to directly transform density increases into refreezing quantities. A study by *Wright et al.* (2007), attempted to quantify refreezing by measuring annual accumulations of superimposed ice on an arctic valley glacier. Superimposed ice forms near the equilibrium line when melt water refreezes at the base of the firn. This method is insufficient in Greenland where the snow facies (dry snow, percolation, wet snow, slush) are much broader than those of a valley glacier and refreezing cannot be accounted for by superimposed ice alone.

Despite the lack of observations of refreezing quantities, estimates are commonly made using parameterizations or models. Refreezing parameterizations are typically used to calculate a maximum quantity of refreezing (Pmax) for a given location via a relatively simple formulation. The simplest parameterization assumes Pmax is some constant percentage of precipitation (*Reeh*, 1991), but more sophisticated formulations calculate Pmax from annual

temperature and precipitation *Pfeffer et al.* (1991). The quantity of melt–water available must also be estimated, as some regions may not attain Pmax if there is not enough melt. Comparisons of the different parameterizations have been made by *Wright et al.* (2007) and *Janssens and Huybrechts* (2000), with the general conclusion that the more sophisticated parameterizations are more accurate.

Fairly complex thermo-mechanical models of snow are also commonly used to estimate refreezing quantities (*Bougamont et al.*, 2005; *Ettema et al.*, 2009; *Fettweis*, 2007; *Greuell and Konzelmann*, 1994; *Mernild et al.*, 2010). These models are typically one–dimensional and divide the snowpack into vertical layers. Heat conduction, infiltration, and refreezing is calculated in each layer, and layer temperatures and permeability determine the quantity of melt water that refreezes at each time step. However, these models have thus far simulated infiltration of melt water as a uniform process without piping or heterogeneous ice lens formation. Given the ubiquity of heterogeneous infiltration in the percolation zone, neglecting to include piping in a physical model may lead to large errors.

With the exception of *Wright et al.* (2007), there has been little independent verification of any published refreezing estimations whether they are based on complex models or parameterizations. Presented here is a new method to estimate refreezing quantities using temperature profiles. This method does not require any hydrologic modeling and therefore avoids the uncertainty associated with piping. The results of the method provide independent estimates of refreezing quantities against which both parameterizations and physical models can be evaluated.

3.2 Methods: Concept

The quantity of water refreezing in the snowpack over a given period of time can be estimated from temperature profiles using conservation of energy. The snowpack is an open system with heat entering and leaving the system at the boundaries via conduction. Additionally, heat is generated within the snowpack when refreezing occurs and releases latent heat. As long as the latent heat is not lost at the boundaries, the total energy in the snow, and

therefore the overall temperature, is equal to the sum of the energy from heat conduction and the energy from refreezing:

$$\text{Total Energy} = \text{Energy Conduction} + \text{Energy Latent Heat (Refreezing)} \tag{3.1}$$

Temperature profiles, used in conjunction with surface temperature data and modeling, enable the calculation of each component of this energy budget. Once the energy from latent heat is found, it is easily converted to a quantity of water using the latent heat of fusion.

3.2.1 Implementation

If heat transfer is considered to be one dimensional and vertical through the snowpack, the total energy gained or lost by the snow over a period of time is related to the temperature change in the snow by:

$$\text{Total Energy} = \int_0^z \Delta T \, \rho(z) \, C \, dz \tag{3.2}$$

Where z is depth, ΔT is the change in snow temperatures over a given period of time, ρ is the density of snow with depth, and C is the heat capacity. Graphically, the total energy gain is equal to the area between an initial and final temperature profile (figure 3.1).

The energy gained or lost from heat conduction over the same time period can be estimated using a heat conduction model. The model is initialized with the initial temperature profile, and the internal temperatures evolve through time in response to the boundary conditions. At the end of the model run, the area between the initial temperature profile and the final model temperature profile is equal to the net energy that was conducted through the boundaries during the model run (figure 3.1).

After the total energy and the energy conducted through the boundaries has been determined, the latent heat can be found using equation 3.1. Rearranging equation 3.1 reveals that the latent heat is equivalent to the area between the final temperature profile (T_f) and the final modeled heat conduction profile (T_c) (figure 3.1):

$$\text{Energy Refreezing} = \int_0^z (T_f - T_c) \, \rho(z) \, C \, dz \tag{3.3}$$

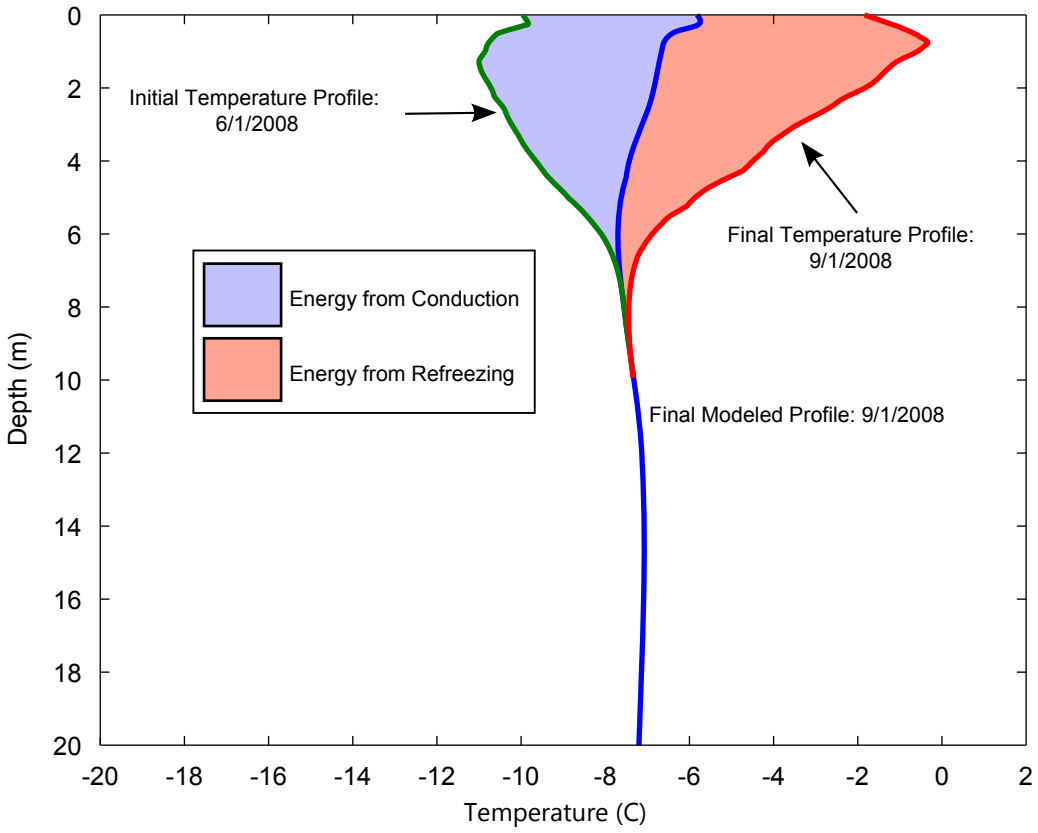

Figure 3.1: Diagram showing the partitioning of heat at site H1. The observed profile on 6/1/2008 is used to initialize a heat conduction model. The area between the final model temperatures on 9/1/2008 and the initial profile is equal to the energy conducted through the boundaries of the snowpack. The area between the model profile and the final profile is equal to the heat released by refreezing over the period 6/1 – 9/1.

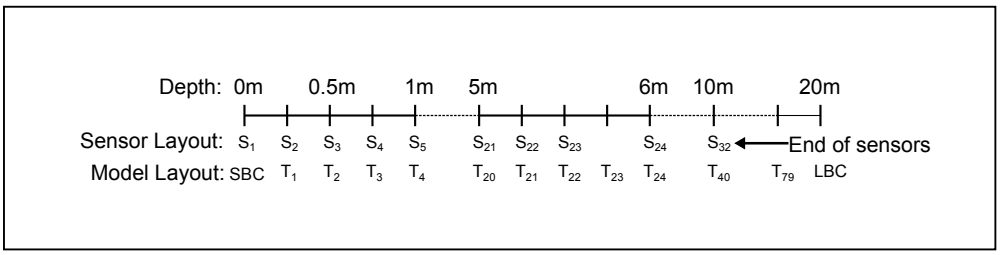

Figure 3.2: Diagram of observed temperature data sensor locations and heat conduction model layout. Most of the model nodes in the upper 10m have a corresponding temperature sensor. The model domain extends 10m beyond the lowest observed temperature sensor.

3.2.2 Method Error

Even if the heat conduction model worked perfectly, there would still be some error associated with this method. Optimally, any increase in the area between the modeled and observed temperature profile resulting from refreezing would be preserved for the duration of the model run. However, since the upper boundary is the same for both the modeled and true profiles, the surface temperature gradients differ between the two profiles. In the summer, the model profile typically gains heat faster than the true profile, while in the winter the model loses heat slower than the true profile. The net effect is that the area between the two curves is almost always decreasing when refreezing is not taking place. This means that the refreezing estimates are really *minimum* estimates. Furthermore, the error due to this heat loss increases with longer model runs. Preliminary testing indicates that the relatively low thermal conductivity of snow limits the magnitude of this error on seasonal timescales such that it does not exceed the overall error from all other sources. It is therefore ignored for now. However, further investigation of the significance of this source of error is warranted.

3.3 Methods: Applied

Heat conduction is modeled at each site using implicit finite difference numerical methods with spatially variable thermal conductivity (Appendix). The firn is modeled to a depth of 20m with 79 equally spaced nodes (0.25m) and an hourly time step (figure 3.2). Most of the temperature node locations in the upper 10m of the model correspond to temperature

sensor locations in the observed data. Temperatures are modeled to 20m depth to minimize the influence of refreezing on the lower boundary condition.

3.3.1 Model Boundary Conditions

We lack the data necessary to complete a surface energy budget to calculate the snow surface temperature at each site for a surface boundary condition (SBC). Instead, the 2m air temperature from the Crawford Point weather station is used as the boundary condition at each site, and is adjusted for elevation via a slope lapse rate. Snow surface temperatures are unlikely to vary much from 2m air temperatures on time scales longer than a few hours (*Serreze and Barry*, 2005). Furthermore, any short-term variations are attenuated quickly in the snowpack due to their high frequency. The surface lapse rates are calculate from monthly average rates compiled by *Hanna et al.* (2005). The lower boundary condition (LBC) at 20m depth, is held constant for the duration of each model run. This value is calculated as an average of the maximum and minimum 10m temperature in the observed data.

3.3.2 Model Initialization

Each model run is initialized using observed temperatures corresponding to the start date and time. The nodal spacing in the model is such that there is a corresponding measured temperature for *almost* every node in the upper 10m of the model domain (figure 3.2). Linear interpolation is used to initialize any node in the upper 10m that lacks a corresponding temperature measurement. The nodes in the lower 10m of the model are initialized using a best-fit quadratic from the lowest three temperatures in the observed data and the LBC.

3.3.3 Model Thermal Conductivities

The thermal conductivities used in the model are calculated from each site density profile. Two slightly different methods were used to relate density to thermal conductivity. The first method uses the Maxwell theoretical relationship between density and thermal conductivity. As detailed in chapter 2, this theoretical relationship shows the best match to the observed

temperature data at most of the sites. However, the data used to calculate thermal conductivities in chapter 2 is primarily from depths greater than 2m where densities are commonly higher than about 450 $\frac{kg}{m^3}$. For the lower density snow in the upper 2m of the snow pack, a lack of bonding and increased transfer of heat by vapor makes the Maxwell model less realistic. A second composite curve was created consisting of the Sturm regression from 0 to 350 $\frac{kg}{m^3}$, the Maxwell model for densities greater than 450 $\frac{kg}{m^3}$, and a linear interpolation in between. The composite curve is not a smooth function, but given the uncertainties in both densities and thermal conductivities, it was deemed sufficient.

3.3.4 Additional Model Components

In addition to the core finite difference model, snow densification and surface height variations are also included in the model. Seasonal densification of snow is most important in the upper snow pack where increases of 30–50% have been measured (*Parry et al.*, 2007). An increase of this magnitude is likely to have a significant affect on thermal conductivities and heat flow. Variations in the location of the surface boundary as a result of accumulations and melting are also profoundly important to transfer of heat within the profile. Winter accumulations insulate the profile from winter heat loss, while summer melting increases the heat flux into the profile. Including these two components helps make the model more realistic and is useful in evaluating model sensitivity.

Densification is implemented by increasing the densities in the upper 2m of the model at a constant rate of 0.1 $\frac{kg}{m^3}$ per hour until the average snow density at the site is reached. This rate corresponds to an approximate increase of 40% over three months for typical snow densities. Surface height variations are determined using CP weather station surface height data. Observed height changes are applied to each site by varying the thickness of the top layer (spacing between the surface boundary and first node). While there is no maximum thickness that the first layer can reach, there is a minimum thickness of 1cm. Increases in surface height are assumed to be accumulations, and the top layer density is therefore also adjusted by averaging in new snow with a density of 200 $\frac{kg}{m^3}$. Lacking the data needed to make a more sophisticated extrapolation of surface height variations, the same raw values

are used at each site along the transect.

3.3.5 Total Heat Calculation

At the end of each model run, the quantity of refreezing in the upper 10m of the snowpack is calculated using a summation to approximate equation 3.

$$\text{Refreezing [m w.e.]} = (\sum (T_{obs} - T_{model})\, \rho(z)\, C\, \Delta z) \frac{1}{H_f\, \rho_w} \tag{3.4}$$

H_f is the latent heat of fusion. It is worth noting the units of each parameter in equation 4:

$$T = [^\circ K] \quad \rho = [\frac{kg}{m^3}] \quad C = [\frac{J}{kg^\circ K}] \quad H_f = 334000[\frac{J}{kg}] \quad \rho_w = 1000[\frac{kg}{m^3}] \quad \Delta z = 0.25[m]$$

Since the spacing of the temperature sensors is greater than the nodal spacing at depths greater than 5.5m (Figure 3.2), linear interpolation is used to calculate an intermediate value so that a change in temperature can be calculated at each of the nodes.

3.3.6 Model Run Configurations

The model can be run at each site with and without densification and surface height variations, as well as, with two different sets of thermal conductivities. The result is 8 different possible model configurations, and the model is run under each configuration at each site. The final refreezing value at each site is the average value from the eight different model runs. The overall error of the method is assessed from the variability of the eight different model runs performed at each site.

The melt season along the transect is estimated to last from late May to September, and the length of the model runs were set to capture this time span as best as possible. However, a lack of data limited the 2007 sites to July – August, and the 2008 sites to June – August (Table 3.1).

3.4 Results

Figure 3.3 shows the average refreezing values at each site with error equal to +/- 2 standard deviations. The values increase with decreasing elevation, as might be expected given

Table 3.1: Model setup and results. Lapse rate [$\frac{^{\circ}C}{km}$], Average/Max/Min refreezing values [cm w.e.], Lower Boundary Condition (LBC) [° C]

Site	Model Run Dates	lapse rate	LBC	Refreeze Ave.	Std. Dev.	Min	Max
CP	6/26/07-9/1/07	N/A	-16.67	3.83	0.25	3.34	4.21
T4	7/3/07 - 8/24/07	6.25	-14.55	7.21	0.26	6.83	7.63
T3	6/28/07 - 9/1/07	6.25	-13.55	8.72	0.42	8.2	9.19
T2-07	6/30/07 - 9/1/07	6.25	-12.2	11.92	0.24	11.55	12.31
T1-07	6/30/07 - 9/1/07	6.25	-10.13	16.83	0.13	16.59	16.97
T2-08	5/28/08 - 9/1/08	6.33	-11.38	1.79	1.26	0.76	3.97
T1-08a	5/30/08 - 9/1/08	6.33	-9.53	4.50	1.34	3.48	6.86
T1-08b	6/1/08 - 9/1/08	6.33	-10	7.34	1.39	5.95	9.32
H1	6/1/08 - 9/1/08	6.33	-7.2	8.47	0.86	7.71	10.22
H163	5/31/08 - 9/1/08	6.33	-6.88	9.17	0.99	7.83	10.99
H165	5/31/08 - 9/1/08	6.33	-6.7	8.05	0.86	6.84	9.64
H2	5/31/08 - 9/1/08	6.33	-2.93	15.23	1.08	13.87	17.23
H3	5/31/08 - 9/1/08	6.33	-3.53	11.61	0.67	10.61	12.75
H4	5/31/08 - 9/1/08	6.33	-6.15	12.32	2.02	9.96	15.2

increased melting with lower elevations. However, there is some indication of a decrease in refreezing values at sites lower than H2. Unfortunately, the error associated with each site makes it difficult to judge the significance of the decrease. The high melt year of 2007 is evident in the refreezing values with a significant decrease in refreezing at sites T2 and T1 in 2008.

3.5 Discussion

As shown in Table 3.1, there is a significant increase in the standard deviations at the 2008 sites over the 2007 sites. One reason for this is the length of the model runs. A more extensive data set at the 2008 sites allows for longer model runs that capture more of the melt season, but this allows more time for errors to accumulate in the output. Additionally, the near surface densities at the 2007 sites are generally higher because the temperature strings were installed later in the melt season after some densification of the snowpack had taken place. This causes the densification component in the model to have less of an effect and, therefore, less variability between model runs. At site T1 in 2008, two temperature strings were installed about 10m apart. While the average values between the two strings

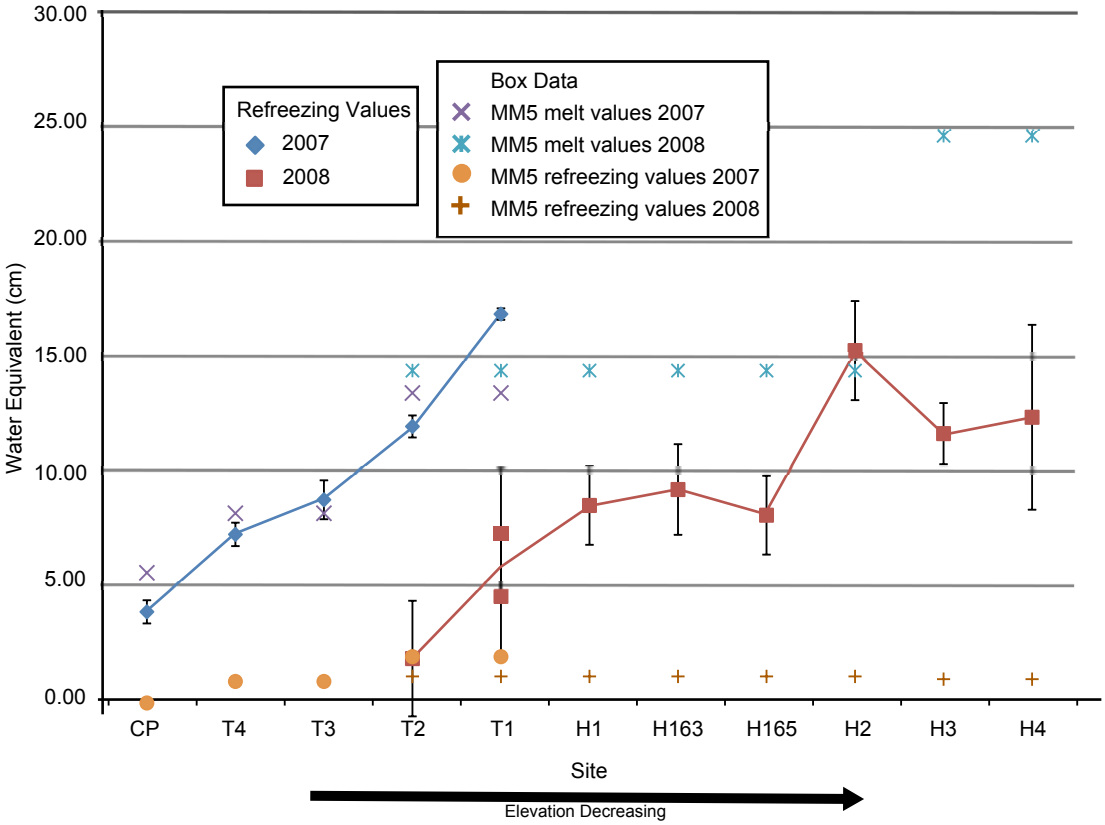

Figure 3.3: Refreezing values at each site compared to melt and refreezing values from RCM Polar MM5. MM5 melt values are similar to my refreezing values, but MM5 refreezing values are, for the most part, significantly different.

are quite different, the error bars overlap. This range of values may be more representative of the true uncertainty at each site.

Also plotted in figure 3.3 are melt and refreezing estimates generated by the regional climate model Polar MM5. The Polar MM5 is like a global climate model, except with a much higher resolution and a limited domain centered over Greenland and Iceland. The MM5 is forced at the boundaries by global climate model data and it calculates surface mass balance components on a 24 km grid. To model refreezing, the MM5 uses the *Pfeffer et al.* (1991) refreezing parameterization. This parameterization determines a maximum refreezing quantity for a given location as a function of the annual temperature, accumulations, and average snow densities (*Box et al.*, 2004). A major weakness of this parameterization is that all refreezing is assumed to take place in the very near surface of the firn. Further details of the Polar MM5 model are given by Box et al. 2004, but model output corresponding to years 2007 and 2008 is previously unpublished and is presented here courtesy Jason Box.

Figure 3.3 shows the melt and refreezing values output by the MM5 for the nearest grid cell containing each site. Several of the sites fall within the same 24km x 24 km cell, especially in the middle of the transect. For this reason, many sites show the same Polar MM5 output values. In general, the MM5 melt values are somewhat similar to my refreezing values at many of the sites, while Polar MM5 refreezing values are almost all significantly lower. The accuracy of the MM5 melt values is likely higher than the accuracy of the MM5 refreezing values since the melt values are based on atmospheric physics and not a relatively simple parameterization. Similar values of melt and refreezing are expected at higher elevation sites where the firn lacks any structural features needed for significant lateral transport of melt water (*Brown et al.*, 2011). Thus, the similarity between melt and refreezing values is evidence that the refreezing values are reasonable. In contrast, the low MM5 refreezing values indicate that the *Pfeffer et al.* (1991) parameterization is unable to accurately estimate refreezing in this area. Finally, the divergence of melt values and the simultaneous decrease of my melt values after site H2 are both indicative of the runoff limit.

3.6 Conclusion

Lacking a direct way to measure refreezing quantities, estimates derived from temperature profiles can provide a useful alternative. Further error analysis needs to be completed before the method can be used systematically, but these results are consistent with expectations given regional melt values. The results presented here also indicate that refreezing parameterizations may be significantly inaccurate. It remains to be seen whether more complex snow models incorporating both hydrology and heat flow provide similar values to those calculated via temperature profiles. Future work could use temperature profile based refreezing estimates as a means of validating any number of parameterizations and snow models currently in use. Accurate refreezing quantities will go a long way towards reducing uncertainty in Greenland mass balance estimates.

Appendix A

A.1 Finite Difference Method

A.1.1 Finite Difference Equations

The following is a derivation (following *Gerya* (2010)) of the *implicit*, conservative finite difference method for numerically approximating the heat equation with variable thermal conductivity. The one dimensional heat equation is commonly given as $\frac{\partial T}{\partial t} = k\frac{\partial^2 T}{\partial x^2}$, where k is the thermal diffusivity $k = \frac{K}{\rho C}$ (ρ is density, C is heat capacity). However, this equation assumes a constant thermal conductivity (K) with space. For a variable thermal conductivity, the heat equation can be written in terms of heat flux as:

$$\rho(x)C\frac{\partial T}{\partial t} = -(\frac{\partial q}{\partial x}) \quad \text{where heat flux } q = -K(x)\frac{\partial T}{\partial x} \tag{A.1}$$

In this formulation, both K and density (ρ) are functions of space, but heat capacity C is constant. The value of $T(x,t)$ can be estimated at certain points called nodes by approximating the partial derivatives at each node.

Figure A.1 shows three nodes in space separated by an amount Δx. A second order approximation of $\frac{\partial q}{\partial x}$ at node n is given by :

$$\frac{\partial q_n}{\partial x} \approx \frac{q_{m+1} - q_m}{\frac{1}{2}(\Delta x_m + \Delta x_{m+1})}$$

q_m is the value of the heat flux at a point in between two nodes and can be approximated by:

$$q_m = -K_m\frac{\partial T}{\partial x} \approx -K_m\frac{T_n - T_{n-1}}{\Delta x_m}$$

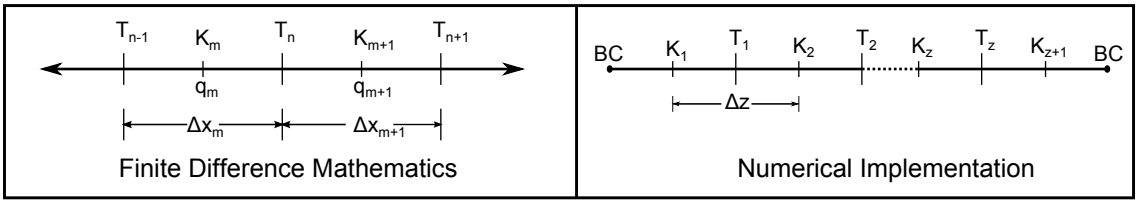

Figure A.1: Diagram showing the geometry of finite difference mathematics and an example of implementing the technique on a domain with z nodes.

When the approximation for q is substituted into the equation it becomes:

$$\frac{\partial q_n}{\partial x} \approx \frac{-K_{m+1}\frac{T_{n+1}-T_n}{\Delta x_{m+1}} + K_m\frac{T_n-T_{n-1}}{\Delta x_m}}{\frac{1}{2}(\Delta x_m + \Delta x_{m+1})}$$

It is important to note that the thermal conductivities used in the approximation correspond to points between the nodes and not the thermal conductivity at the node itself. This is the correct formulation that conserves heat (*Gerya*, 2010). A first order approximation to the partial derivative of temperature with time at node n is given by:

$$\frac{\partial T}{\partial t} \approx \frac{T_{n,t+\Delta t} - T_{n,t}}{\Delta t}$$

Substituting the partial derivative approximations back into equation 1 yields the finite difference equation at node n:

$$\rho_n C\frac{T_{n,t+\Delta t} - T_{n,t}}{\Delta t} = -(\frac{-K_{m+1}\frac{T_{n+1}-T_n}{\Delta x_{m+1}} + K_m\frac{T_n-T_{n-1}}{\Delta x_m}}{\frac{1}{2}(\Delta x_m + \Delta x_{m+1})}) \tag{A.2}$$

A.1.2 Solving Finite Difference Equations

In order to solve the finite difference equation (equation A.2) at each node, for each step in time, the temperature must be known at every node at $t = 0$. This is known as an initial condition. Equation A.2 cannot be solved at the endpoint nodes. Instead the temperature at the boundary, the boundary condition (BC), must be specified at each time step. With boundary values and initial conditions, the temperature at each node $T_{n,t}$ is known and equation 3.2 can be used to solve for $T_{n,t+\Delta t}$ directly. This is known as the *explicit* finite difference solution. However, if the nodes on the right hand side of equation A.2 are considered to correspond to $t + \Delta t$ rather than t, $T_{n,t+\Delta t}$ can still be solved using a system of equations.

This technique is known as the *implicit* finite difference solution and has the benefit of being a more stable solution at longer time steps.

A.1.3 Implementation

The following demonstrates the implicit finite difference technique applied to a domain with z temperature nodes (figure A.1). The finite difference equation at temperature node T_z is given by:

$$\rho_z C \frac{T_{z,t+\Delta t} - T_{z,t}}{\Delta t} = -(\frac{-K_{z+1}\frac{T_{z+1}-T_z}{\Delta z} + K_z\frac{T_z-T_{z-1}}{\Delta z}}{\Delta z}) \tag{A.3}$$

While not shown in the equation above, the implicit method considers all nodes on the right hand side of the equation to be at $t + \Delta t$. Rearranging equation A.3 yields:

$$T_{z,t} = \frac{\Delta t}{\rho_z C(\Delta z)^2}(-K_{z+1}T_{z+1} + K_{z+1}T_z + K_z T_z - K_z T_{z-1}) + T_z$$

Again, for clarity, all the T variables on the right hand side of the equation are at $t + \Delta t$. The final simplified *implicit* finite difference equation is:

$$T_{z,t} = -\beta_z K_{z+1} T_{z+1,t+\Delta t} + [\beta_z(K_{z+1} + K_z) + 1]T_{z,t+\Delta t} - \beta_z K_z T_{z-1,t+\Delta t} \tag{A.4}$$

$$\text{Where } \beta_z = \frac{\Delta t}{\rho_z C(\Delta z)^2}$$

Applying equation 4 at each node yields a system of equations of the form $\mathbf{A}x = b$:

$$\begin{bmatrix} X_1 & J_1 & 0 & \dots & 0 \\ Y_2 & X_2 & J_2 & \ddots & \vdots \\ 0 & \ddots & \ddots & \ddots & 0 \\ \vdots & \ddots & \ddots & \ddots & J_{z-1} \\ 0 & \dots & 0 & Y_z & X_z \end{bmatrix} \begin{bmatrix} T_{1,t+\Delta t} \\ \vdots \\ \vdots \\ \vdots \\ T_{z,t+\Delta t} \end{bmatrix} = \begin{bmatrix} T_{1,t} - Y_1(\text{SBC}_{t+\Delta t}) \\ T_{2,t} \\ \vdots \\ T_{z-1,t} \\ T_{z,t} - J_z(\text{LBC}_{t+\Delta t}) \end{bmatrix} \tag{A.5}$$

$$\text{Where } X_z = \beta_z(K_{z+1} + K_z) + 1 \quad Y_z = -\beta_z K_z \quad J_z = -\beta_z K_{z+1}$$

At the endpoints the boundary conditions must be included in the solution vector b. It is important to note that the boundary conditions correspond to time $t + \Delta t$. Thus the temperature at time $t + \Delta t$ at node z can be found by solving $\mathbf{A}x = b$.

A.2 Vector Norm

A 'norm' is a measure of the length of a vector (*Aster et al.*, 2005). One of the most familiar norms is the 2–norm, or the Euclidian length. The 2–norm is defined by:

$$\|\mathbf{x}\|_2 = \sqrt{x_1^2 + x_2^2 + x_3^2 + \cdots + x_n^2}$$

For a two dimensional vector, the 2-norm is simply the Pythagorean Theorem. The 1–norm is also commonly used and is defined by:

$$\|\mathbf{x}\|_1 = |x_1| + |x_2| + |x_3| + \cdots + |x_n|$$

A.3 Theoretical Snow Thermal Conductivity Models

The thermal conductivity of snow as a function of density can be estimated theoretically by modeling the snow as a combination of ice and air arranged in a predictable geometry. The idealized geometry enables the analytical calculation of the heat flow through the system at steady state. The bulk heat flow through the system can then be characterized by an equivalent thermal conductivity (K_{eq}). Analytical solutions exist for only relatively simple geometries and therefore theoretical models are utilized more for understanding than for prediction. Furthermore, most theoretical models do not include latent heat transfer.

Two of the most simple models are the parallel and series plate models. These models are considered to be opposite extremes in terms of heat flow and act as boundaries on the density-thermal conductivity solution space. The series model provides a lower bound on thermal conductivity and the parallel model the upper bound. Both models approximate the snow pack as a series of laterally infinite plates of ice separated by layers of air. In the series plate model, heat flow is perpendicular to the plates, while in the parallel model heat flow is parallel to the plates (Figure A.2). As demonstrated in the derivations below, the parallel and series models are equivalent to combining electrical conductors in parallel and series.

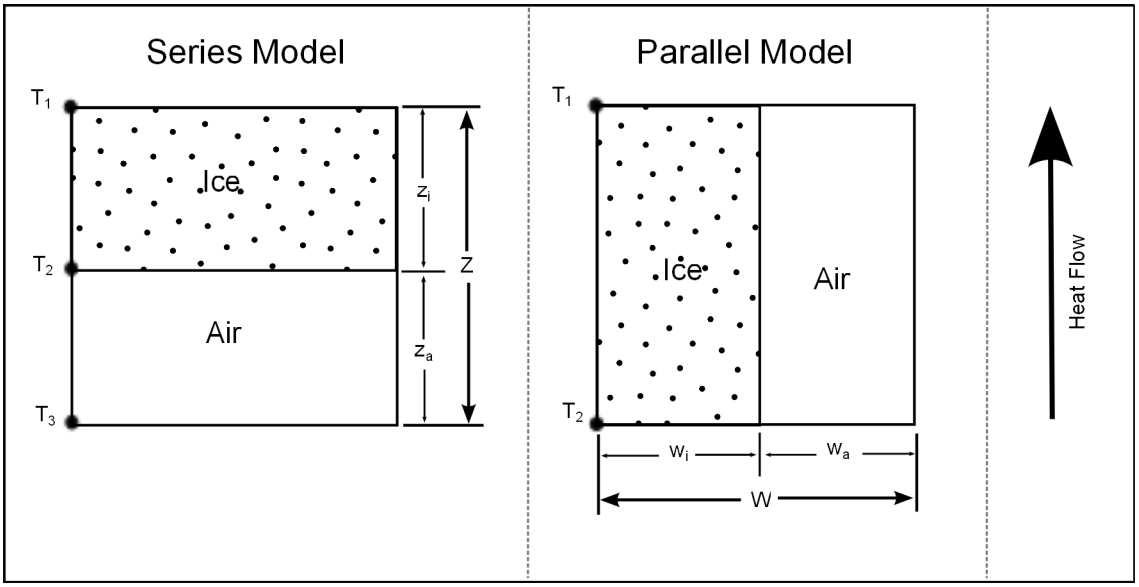

Figure A.2: Series and Parallel Plate models

A.3.1 Series Plate Model Derivation

As shown in figure A.2, a layer of air and a layer of ice are oriented perpendicular to heat flow. The absolute size of the layers is unimportant mathematically, but in a qualitative sense, the layers must be small enough to be in local steady state regardless of the temperature variations across the bulk of the snow. At the boundaries of each layer are temperatures T_1, T_2 and T_3. Since the system is in steady state, the heat flux through each layer is equal.

$$\frac{T_2 - T_1}{z_i} K_i = \frac{T_3 - T_2}{z_a} K_a = Q \tag{A.6}$$

To determine an equivalent thermal conductivity (K_{eq}) for the system, the heat flux through the system is calculated:

$$Q = \frac{T_3 - T_2}{Z} K_{eq} \tag{A.7}$$

Solving for T_2 using equation 6 and then plugging the result into equation 7 yields the following:

$$\frac{\frac{K_a z_i T_3 + K_i z_a T_1}{K_i z_a + K_a z_1} - T_1}{z_i} K_i = \frac{T_3 - T_2}{Z} K_{eq}$$

Solving for K_{eq} via copious amounts of algebra yields:

$$K_{eq} = \frac{1}{(\frac{z_a}{Z})(\frac{1}{K_a}) + (\frac{z_i}{Z})(\frac{1}{K_i})}$$

The relative thickness of the layers $(\frac{z}{Z})$ can be related to the snow density and the final formula for K_{eq} as a function of snow density is:

$$K_{eq} = \frac{1}{(1 - \frac{\rho_s}{\rho_i})(\frac{1}{K_a}) + (\frac{\rho_s}{\rho_i})(\frac{1}{K_i})} \tag{A.8}$$

A.3.2 Parallel Plate Model Derivation

In the Parallel Plate model, heat flow is parallel to the plates of ice. Since there is no lateral heat flow in the model, the temperature gradient must be equal in both the air and the ice. However, the heat flux is different between the air and the ice due to different thermal conductivities. The total heat flow through the system is the sum of the heat flow along each flow path:

$$TotalHeatFlux = \int_0^{w_i} \frac{T_2 - T_1}{Z} K_i dw + \int_0^{w_a} \frac{T_2 - T_1}{Z} K_a dw \tag{A.9}$$

Solving the integrals and setting the resulting heat flux equal to the heat flux through the system using K_{eq}:

$$\frac{T_2 - T_1}{Z} K_{eq} = \frac{T_2 - T_1}{Z} (\frac{w_i}{W} K_i + \frac{w_a}{W} K_a)$$

Changing the relative ice and air widths $(\frac{w}{W})$ to densities as was done in the series model and solving for K_{eq}:

$$K_{eq} = \rho_s (\frac{K_i - K_a}{\rho_i}) + K_a \tag{A.10}$$

References

Armstrong, R., and E. Brun (2008), *Snow and Climate: Physical Processes, Surface Energy Exchange, and Modeling*, Cambridge University Press.

Arons, E., and S. Colbeck (1995), Geometry of heat and mass transfer in dry snow: theory and experiment, *Geophysical Reviews*, pp. 463–493.

Aster, R., B. Borchers, and C. Thurber (2005), *Parameter Estimation and Inverse Problems*, Elsevier.

Benson, C. (1962), Stratigraphic studies in the snow and firn of the greenland icesheet, *Cold Regions Research and Engineering Laboratory - Research Report 70*.

Bougamont, M., J. L. Bamber, and W. Greuell (2005), A surface mass balance model for the greenland ice sheet, *Journal of Geophysical Research*, *110*, doi:10.1029/2005JF000348.

Box, J., D. Bromwich, and L. Bai (2004), Greenland ice sheet surface mass balance 1991-2000: Application of polar mm5 mesoscale model and in situ data, *Journal of Geophysical Research*, *109*, doi:10.1029/2003JD004451.

Box, J., D. Bromwich, B. Veenhuis, L. Bai, J. Stroeve, J. Rogers, K. Steffen, T. Haran, and S. Wang (2006), Greenland ice-sheet surface mass balance variability (1988-2004) from calibrated polar mm5 output, *Journal of Climate*, *19*(12), 2783–2800.

Brandt, R., and S. Warren (1997), Temperature measurements and heat transfer in near surface snow at the south pole, *Journal of Glaciology*, *43*(144), 339–351.

Brown, J., J. Harper, W. Pfeffer, N. Humphrey, and J. Bradford (2011), High resolution study of layering within the percolation and soaked facies of the greenland icesheet, *Annals of Glaciology*, *52*(59), 35–42.

Carson, J., S. Lovatt, D. Tanner, and A. Cleland (2005), Thermal conductivity bounds for isotropic, porous materials, *International Journal of Heat and Mass Transfer*, *48*, 2150 – 2158.

Cuffey, K., and W. Paterson (2010), *The Physics of Glaciers*, 4th ed., Elsevier.

Ettema, J., M. van den Broeke, E. van Meijgaard, W. van de Berg, J. Bamber, J. Box, and R. Bales (2009), Higher surface mass balance of the greenland ice sheet revealed by high resolution climate modeling, *Geophysical Research Letters*, *36*, doi:10.1029/2009GL038110.

Ettema, J., M. van den Broeke, E. van Meijgaard, W. van de Berg, J. Box, and K. Steffen (2010), Climate of the greenland ice sheet using a high resolution climate model – part 1: Evaluation, *The Cryosphere*, *4*, 511–527.

Fettweis, X. (2007), Reconstruction of the 1979–2006 greenland ice sheet surface mass balance using the regional climate model mar, *The Cryosphere*, *1*, 21–40.

Finsterwalder, R. (1959), Expedition glaciologique internationale au groenland 1957-60 (e.g.i.g.), *Journal of Glaciology*, *3*, 542–546.

Gerya, T. (2010), *Introduction to Numerical Geodynamic Modelling*, Cambridge University Press.

Greuell, W., and T. Konzelmann (1994), Numerical modelling of the energy balance and the englacial temperature of the greenland ice sheet. calculations for the eth-camp location (west greenland, 1155 m a.s.1.), *Global and Planetary Change*, *9*, 91–114.

Hanna, E., P. Huybrechts, I. Janssens, J. Cappelen, K. Steffen, and A. Stephens (2005), Runoff and mass balance of the greenland ice sheet: 1958 – 2003, *Journal of Geophysical Research*, *110*, doi:10.1029/2004JD005641.

Hanna, E., J. McConnell, S. Das, J. Cappelen, and A. Stephens (2006), Observed and modeled greenland ice sheet snow accumulation, 1958-2003, and links with regional climate forcing, *Journal of Climate*, *19*, 344–358.

Harper, J., N. Humphrey, T. Pfeffer, and J. Brown (2011), Firn stratigraphy and temperature to 10 m depth in the percolation zone of western greenland, 2007-2009, *INSTAAR Occasional Paper*, (60).

Hornberger, G., J. Raffensperger, P. Wilberg, and K. Eshleman (1998), *Elements of Physical Hydrology*, John Hopkins University Press.

Humphrey, N., J. Harper, and W. Pfeffer (2012), Thermal tracking of melt water retention in greenland's accumulation area, *Journal of Geophysical Research*, *112*, doi: 10.1029/2011JF002083.

Janssens, I., and P. Huybrechts (2000), The treatment of melt-water retention in mass-balance parameterizations of the greenland ice shee, *Annals of Glaciology*, *31*, 133–140.

Mernild, S., G. Liston, C. Hiemstra, and J. Christensen (2010), Greenland ice sheet surface mass balance modeling in a 131-yr perspective, *Journal of Hydrometeorology*, pp. 3–25, doi:10.1175/2009jhm1140.1.

Parry, V., P. Nienow, D. Mair, J. Scott, B. Hubbard, K. Steffen, and D. Wingham (2007), Investigations of meltwater refreezing and density variations in the snowpack and firn within the percolation zone of the greenland ice sheet, *Annals of Glaciology*, *46*, 61–68.

Pfeffer, T., M. Meier, and T. Illangasekare (1991), Retention of greenland runoff by refreezing: implications for projected future sea level change, *Journal of Geophysical Research*, *96*, 22,117–22,124.

Pfeffer, W., and N. Humphrey (1996), Determination of timing and location of water movement and ice layer formation by temperature measurements in sub-freezing snow, *Journal of Glaciology*, *42*, 292–304.

Pfeffer, W., and N. Humphrey (1998), Formation of ice layers by infiltration and refreezing of meltwater, *Annals of Glaciology*, *26*, 83–91.

Reeh, N. (1991), Parameterization of melt rate and surface temperature on the greenland ice sheet, *Polarforschung*, *59*, 113–128.

Rignot, E., I. Velicogna, M. van den Broeke, A. Monaghan, and J. Lenaerts (2011), Acceleration of the contribution of the greenland and antarctic icesheets to sea level rise, *Geophysical Research Letters*, *38*(L05503), doi:10.1029/2011GL046583.

Schwerdtfeger, P. (1963), Theoretical derivation of the thermal conductivity and diffusivity of snow, *General Assembly of Berkeley Commission of Snow and Ice*, *61*, 75–81.

Serreze, M., and R. Barry (2005), *The Arctic Climate System*, Cambridge University Press.

Steffen, K., J. E. Box, and W. Abdalati (1996), Greenland climate network: Gc-net, in *CRREL 96-27 Special Report on Glaciers, Ice Sheets and Volcanoes, trib. to M. Meier*, edited by S. Colbeck, pp. 98–103.

Sturm, M., J. Holmgren, M. Konig, and K. Morris (1997), The thermal conductivity of seasonal snow, *Journal of Glaciology*, *143*, 26–41.

Tedesco, M., X. Fettweis, M. van den Broeke, R. van de Wal, C. Smeets, W. van de Berg, M. Serreze, and J. Box (2011), The role of albedo and accumulation in the 2010 melting record in greenland, *Environmental Research Letters*, *6*, 1–6.

Van den Broeke, M., J. Bamber, J. Ettema, E. Rignot, E. Schrama, W. van de Berg, E. van Meijgaard, I. Velicogna, and B. Wouters (2009), Partitioning recent greenland mass loss, *Science*, *326*, 984–986.

Wright, A. P., J. L. Wadham, M. J. Siegert, A. Luckman, J. Kohler, and A. M. Nuttall (2007), Modeling the refreezing of meltwater as superimposed ice on a high arctic glacier: A comparison of approaches, *Journal of Geophysical Research*, *112*, doi:10.1029/2007JF000818.